

## **Response to the reviewers**

We thank all three reviewers for their positive reviews and constructive comments. We have revised the manuscript as described in detail below, and we hope that we have dealt with all suggestions in an adequate manner.

### **Anonymous Referee #1**

Werner et al., present first results of the newly developed isotope-enabled version of the Earth System Model ECHAM5/MPI-OM. They focused on two equilibrium simulations under the pre-industrial and last glacial maximum period and compare the model results with observational data and paleoclimate records in the atmospheric/continental and oceanic components. Overall, isotope variations ( $\delta^{18}\text{O}$ ,  $\delta\text{D}$ ) for the PI and LGM climate are in good agreement with available data, although some bias are identified and discussed in the manuscript. The paper is well write, clear and the results interesting. In particular, the authors highlight interesting results that could be further explored in the future. Among them, the assessment of the stability of the  $\delta$ -T relation for LGM-PI climate changes reveals that the temporal  $\delta$ -T gradient might have been substantially lower than the modern spatial one for most mid- to high-latitudinal regions. Such a deviation could indeed cause a strong bias in the “classical”  $\delta$ -paleothermometry approach. Also, the remarkable improvement in modelling the deuterium excess signal allows to question the approach by Merlivat and Jouzel (1979), question the cooling of SST during the LGM and support the “classical” interpretation of dex changes in Antarctic ice cores as a proxy for SST changes in the source regions of water transported to Antarctica. I think this paper is suitable for publication in GMD and I recommend publication after the authors have adressed the moderate/minor comments below.

Comments:

1) page 8837 Lines 15-19 : Some studies concerning Chinese speleothem suggest that  $\delta^{18}\text{O}$  variations reflect changes to regional moisture sources and the intensity or provenance of atmospheric transport pathways (LeGrande and Schmidt, 2009; Dayem et al., 2010; Lewis et al., 2010; Maher and Thompson, 2012; Caley et al., 2014; Tan, 2014).

We have added these findings and the related references in the revised manuscript.

2) page 8841 lines 25-26 : “under pre-industrial and LGM, defined as the period 23 000–19 000 years before present” A reference is needed here.

We have decided to delete “defined as the period 23 000–19 000 years before present” as we realized that this has been a misleading statement in this part of the paper.

For the LGM simulation, glacial boundary conditions correspond to 21ka B.P. in accordance with PMIP3 rules, while the different LGM data from ice cores, speleothems, and marine records has been selected from the period 23ka -19ka (22ka-19ka for speleothems). This selection is described in detail in Chapter 3.2-3.4.

3) page 8846 line 12 : “with a prescribed glacial increase of  $\delta^{18}\text{O}$  of +1 ‰ ( $\delta\text{D}$ : +8 ‰” Here, the authors prescribed a glacial increase of 8 ‰ in  $\delta\text{D}$  for the LGM period.

According to Schrag et al., 2002, the glacial increase would be around 7.2‰. Also, if all the GISS data (depth < 3000 meters) (Schmidt et al., 1999) are used, the present day relationship between  $\delta^{18}\text{O}$  and  $\delta\text{D}$  give a glacial  $\delta\text{D}$  increase of 7.3‰ for a  $\delta^{18}\text{O}$  value of 1‰ (assuming that this relationship is still valid during the LGM). Therefore, the two independent approaches lead to a  $\delta\text{D}$  increase of 7.2‰ rather than 8‰ during the LGM. What could be the implications of such a different value on the deuterium excess calculation presented in this manuscript in part 4.2.4?

A mean glacial ocean  $\delta\text{D}$  increase of +7.2‰ instead of +8‰ would lead to a small glacial decrease of the mean deuterium excess signal in the ocean of -0.8‰. As a first-order estimate, one can assume that such lowered deuterium excess signal in the ocean will lead to an equivalent lower deuterium excess value both in vapour above the ocean and, consequently, in precipitation, too. We have added these considerations in Chapter 4.2.4.

4) page 8848-8849 Kim and O'Neil 1997 equation. I don't understand how the data-model comparison is done. Does the authors have used the temperature in the model and the  $\text{d}^{18}\text{O}$  of the calcite from speleothem data to calculate a  $\text{d}^{18}\text{O}_{\text{water}}$  value and then compare this to model values in Figure 1? On figure 1, there is only a scale of  $\text{d}^{18}\text{O}$  in precipitation and the speleothem records are included. Please explain in more details how the  $\text{d}^{18}\text{O}_{\text{water}}$  of speleothems are calculated (which temperature values are used?).

We thank the reviewer for this very helpful comment. For the conversion of modern  $\delta^{18}\text{O}_{\text{c}}$  of calcite from the selected speleothem sites (Table 2) to a  $\delta^{18}\text{O}_{\text{p}}$  water value shown in Fig. 1, we have used annual mean ERA40 soil temperatures (ERA40 variable soil temperature, layer #1) averaged over the period 1961-1990. We have forgotten to mention this detail in our original manuscript but it is now explicitly stated in part 4.1.1.

In the legend of the figure 1, the Table 1 and Table 2 do not refer to the corresponding dataset, please inverse.

Corrected.

On Figure 8, I am again confused because the speleothem data are presented in green on a  $\text{d}^{18}\text{O}_{\text{precipitation}}$  scale but the figure caption mention that the  $\text{d}^{18}\text{O}_{\text{calcite}}$  changes are shown. I recommend to use atmospheric temperature to calculate the  $\text{d}^{18}\text{O}_{\text{p}}$  of speleothem and then plot this on figure 1 or 8. Alternatively, the authors could separate the speleothems data and compare the  $\text{d}^{18}\text{O}_{\text{calcite}}$  data with  $\text{d}^{18}\text{O}_{\text{calcite}}$  of the model (calculate from temperature and  $\text{d}^{18}\text{O}_{\text{p}}$  from the model) as it was done for marine carbonates.

We are sorry for this confusion. For the model-data comparison of the LGM-PI speleothem data, we have calculated the simulated LGM-PI change of  $\delta^{18}\text{O}_{\text{c}}$  in calcite, using both modelled  $\delta^{18}\text{O}_{\text{p}}$  in precipitation and surface temperatures for the PI and LGM climate, as it was done for marine carbonates. Thus, the axis labels of Fig 8b were erroneous as were compare both model vs. reconstructed  $\delta^{18}\text{O}_{\text{p}}$  anomalies (for ice cores) and  $\delta^{18}\text{O}_{\text{c}}$  anomalies (for speleothems) in the same scatter plot. The labels and figure caption of Fig. 8 have been corrected and we now describe this comparison in more detail in paragraph 4.2.2.

5) Page 8849 Shackleton (1974) equation. There is a conversion between the two scale (PDB and SMOW): expressed as  $d180_{water(VPDB)} = d180_{water(VSMOW)} - 0.27$  (Hut, 1987) that is not describe here and that is necessary.

This information is now added to paragraph 3.4

6) Conclusion part, page 8866, line 29 "CLIMAP". I think this is cooler than MARGO, not CLIMAP.

Corrected.

7) Figure 4 : "arbitrary subset of 300 data". I rather suggest to the authors to revise the figure and show the model results without data on a new panel a) and add on a secondary panel with all the GISS data (Atlantic Ocean:  $n = 5811$ , Pacific Ocean:  $n = 2985$ ) with or without model results. The comparison between model and all the GISS data will be possible with readability.

We have revised Figure 4 as suggested. The figure now includes two new panels c) and d) that display all available GISS data for the Atlantic and Pacific Ocean. The figure caption is changed, accordingly.

### **Anonymous Referee #2**

The manuscript by Werner and co-authors presents first results on the pre-industrial and LGM conditions of a coupled ocean-atmosphere model equipped with water isotopes. The spatial repartition of  $d180$  and  $d$ -excess in the ocean and atmosphere is systematically confronted to available data for both periods with a general good match between model and data. The manuscript is very well written and provides all the necessary details in the text and in the figures for the general reader. The number of figures is quite high but I would recommend keeping all of them. I only have minor comments and I recommend publications of the manuscript:

-p. 8840, l.4: it would be nice to quote also the 2013 paper by Risi and co-authors on  $170$ -excess modeling.

The reference has been added to the text.

- p. 8843, l.22: The authors neglect as often done (but not always) the possible fractionation during evapotranspiration processes from terrestrial areas. It would be nice to expand a bit more the possible implications of such hypothesis on  $d180$  and especially  $d$ -excess in regions where the fractionation during evaporation of terrestrial water may become important (e.g. Amazonian basin following the suggestion of Gat and Matsui (1991)).

In Haese et al. (2013) we have analysed in detail the implications of a potential fractionation during evapotranspiration processes on the  $\delta^{18}O$  and deuterium excess signal in different water reservoirs. We found no large effect of such fractionation processes on the  $\delta^{18}O$  and  $d$ -excess signal in precipitation, but a potential large change

of the isotopic composition of soil water by several per mill (see Haese et al., 2013, Fig. 8). Such change might be especially relevant for paleoclimate records, where the isotope signal reflects changes in the soil water (e.g., speleothems, ancient groundwater). However, it remains an open question if such changes would also affect the simulated glacial anomalies ( $\Delta_{\text{LGM-PI}} \delta^{18}\text{O}$ ,  $\Delta_{\text{LGM-PI}} \text{dex}$ ), or simply lead to an equivalent strong change of  $\delta^{18}\text{O}$  and dex for both the PI and LGM simulations (without a glacial anomaly change as compared to our chosen model setup). These considerations are now added to Chapter 2.

- In general, I think that some explanations on the added value of the coupled model compared to the atmosphere only model for the modeling of  $\delta^{18}\text{O}$  and d-excess in precipitation should be given in introduction of the manuscript.

We have added some more arguments for using a fully coupled isotope GCM in Chapter 1.

- p. 8848, l. 8, replace “is” by “are”

Corrected.

- Figure 6a and corresponding text p. 8854: what do you mean exactly by isotopic values in “evaporation” ? do you mean water vapor or evaporation flux ? It would be nice to clarify since only isotopic values in water vapor can be compared to data.

In Fig. 6a, the annual mean deuterium excess values in the evaporation flux are plotted. As mentioned in the text, we are aware that this quantity is difficult to evaluate, as it has not been measured, yet. However, we prefer to show it as a counterpart to the deuterium signal in the precipitation flux (Fig. 6b). Furthermore, the deuterium excess in evaporation has recently been reconstructed by Pfahl and Sodemann (2014) and the ECHAM5-wiso results can be compared to their results. This is now explicitly mentioned in the revised manuscript.

- p 8856, l. 6: A good way to test the Merlivat and Jouzel (1979) formulation would be to look at the modeled slope between d-excess in the water vapor above the ocean and relative humidity. How does this compare to the Merlivat and Jouzel (1979) slope ?

For the region 60°S-60°N we calculate a slope  $m$  between d-excess in the vapour layer above the ocean and the related relative humidity of  $m = -6.3\text{‰}/(10\% \text{ rel. humidity change})$ . This is very close to the value of  $-6\text{‰}/(10\% \text{ rel. humidity change})$  given in Merlivat and Jouzel (1979). We have added this information to the manuscript.

- I am quite convinced by the discussion on the influence of SST on d-excess presented on p. 8864. Still, it would be nice to justify further why the relative humidity of the source relative humidity was not different by more than 5% in the LGM compared to the pre-industrial situation.

The rather small variations of the LGM relative humidity changes are somewhat surprising, as cooler SST should lead to cooler air temperatures above the ocean surface, which then should lead to higher relative humidity levels (if the amount of water in the air stays constant). However, we find in our simulation that the air directly above the

ocean surface cools slightly stronger during the LGM than the SST themselves. This leads to a reduced glacial evaporation flux from the ocean to the atmosphere, which decreases the relative humidity of the vapour and counterbalance the first effect.

Similar small changes of relative humidity changes above the ocean surface and the counterbalance of different effects have recently been reported for a set of CMIP5 climate model results by Laîné et al. (2014). They have analysed a future water climate, though.

### **Anonymous Referee #3**

Summary: The authors present results from a pre-industrial and Last Glacial Maximum simulation of climate using the isotope enabled version of the coupled ocean-atmosphere model ECHAM5/MPI-OM. This is a sound manuscript. I would suggest it requires only rather minor revisions before publication.

Major comments: I have only one more major comment which is on section 4.2.4 “Glacial changes of the deuterium excess”. It is really interesting that the authors find that glacial sea surface temperature which are cooler than the GLAMAP reconstruction, lead to an improved simulation of dex changes over Antarctica. Would it be possible to also comment on whether coupled model ECHAM5 simulation of sea ice around Antarctica is also in agreement with the available sea ice data e.g. from Gersonde et al.?

The simulated sea ice of the COSMOS LGM simulation has already been described in detail in Zhang et al. (2013) and our simulation results are comparable to this previous study. For the southern hemisphere, there is a reasonable agreement between the simulated sea ice concentration and proxy data by Gersonde et al. (2005), such as the austral winter sea ice extent in the Atlantic sector and the austral summer sea ice extent in the Indian ocean sector. However, our LGM simulation underestimates a larger extent of sporadic summer sea ice between 5°E and 5°W in the Southern Ocean, as reported by Gersonde et al. (2005).

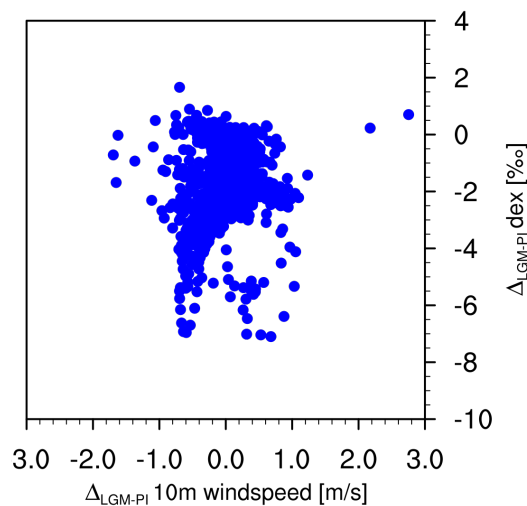
Compared to GLAMAP, we find a much reduced sea ice cover in austral summer. This might lead to a stronger contribution of vapour stemming from regions between 60°-65°S to the Antarctic ice sheet. As vapour from these regions has a strong negative dex signal (cf. Fig. 12) such shift in the contribution might lead to a more negative deuterium excess signal in precipitation, too. These considerations are now added to the manuscript (part 4.2.4.).

Whilst plotting simulated changes of dex in vapour against the modelled relative humidity change between LGM and PI over the ocean surface reveals no correlation between these humidity changes and the simulated dex variations in the vapour layer, these are over rather large changes in climate, with many changes in climate variables. Some work, such as that by Schmidt and LeGrande using the gissE model, indicates that near surface wind changes may also be important in dex changes. Examining the correlation and relationship between dex and relative humidity, and dex and SST does not eliminate the possibility that the dex-SST relationship could be dependent on other aspects of the climate shift – such as wind speed changes. It would therefore be useful if

the authors could support their dex-SST relationship assertion by providing a much wider examination of dex-climatic variable relationships.

Our intention of analysing the dex relation vs. relative humidity and SST changes was to simply test the recent hypothesis of Pfahl and Soedemann (2014) regarding an improved interpretation of dex variations in ice core records. Of course, we fully agree that the shown correlation between dex and SST changes does not rule out other factors, like wind speed changes, which could affect both dex and SST changes. (However, we do not find a clear correlation between the simulated annual mean glacial 10m windspeed anomalies and the dex signal in the vapour above the surface; see Figure below). These considerations are now mentioned in the manuscript.

More sensitivity studies and analyses are certainly required to explain the simulated glacial dex changes both in vapour and Antarctic precipitation in more detail. We think that such analyses are well beyond the general scope of this manuscript (which is a first, rather general presentation of this new fully-coupled isotope model setup). Thus, we prefer to perform such wider examination of dex-climatic variable relationships in a separate future study, and hope that this decision is adequate.



Minor comments:

P8837 L15 “the combination of water isotopic ratios permits to have a tracer of the low latitudes in polar ice cores” provide a reference, and perhaps make the reference to d-excess more explicit?

We have added 2 references here but do not explicitly mention the deuterium excess at this point, as we discuss this quantity in detail just a few lines below (p.8838, line 4ff.)

P8838 L2 “that they allow reconstructing the three-dimensional structure” rephrase, for example “the reconstruction of” would be better.

Rephrased as suggested.

Section 4.1 Might be better to also include a present day simulation. This would enable the authors to also test the simulation against isotopes in vapour satellite data.

In several previous studies, we have evaluated present-day simulations of the atmospheric model, ECHAM5-wiso, in detail. Some of these studies also included a comparison of model results to available satellite vapour observations both on a global and regional scale (e.g., Werner et al., 2011; Butzin et al, 2014). As the overall results of the coupled ECHAM5/MPI-OM setup are very similar to these previous atmosphere-only ECHAM5 simulations, we decided against a duplication of such detailed present-day vapour data analysis in this study, but rather focus on the simulated modern vs. glacial isotope changes. We hope that this decision is acceptable for the reviewer.

P8864 L1 “constraint”

Corrected.

### **Additional remark**

Very recently, the supercomputer at AWI, which has been used for conducting the presented simulations, has been replaced by a new machine. For future work and consistency, we have decided to prolong both the PI and LGM simulation to a total of 1,500 simulation years (before: PI experiment: 1,400yrs, LGM experiment: 1,300yrs) using this new hardware configuration. In the revised manuscript, we now present the results of the last 100 simulation years (year 1,400-1,499) of both prolonged simulations.

None of the originally submitted results has been affected by this prolongation, but some calculated quantities (mean values, RMSE, isotope slopes, etc.) have slightly changed.

All figures have been updated, too. Only a few of them display very minor changes in global isotope distributions with respect to the previous figure versions.

### **References**

- Gersonde, R., Crosta, X., Abelmann, A. and Armand, L.: Sea-surface temperature and sea ice distribution of the Southern Ocean at the EPILOG Last Glacial Maximum - A circum-Antarctic view based on siliceous microfossil records, *Quaternary Sci Rev*, 24(7-9), 869–896, doi:10.1016/j.quascirev.2004.07.015, 2005.
- Haese, B., Werner, M. and Lohmann, G.: Stable water isotopes in the coupled atmosphere–land surface model ECHAM5-JSBACH, *Geosci. Model Dev.*, 6(5), 1463–1480, doi:10.5194/gmd-6-1463-2013, 2013.
- Laîné, A., Nakamura, H., Nishii, K. and Miyasaka, T.: A diagnostic study of future evaporation changes projected in CMIP5 climate models, *Clim. Dyn.*, 42(9-10), 2745–2761, doi:10.1007/s00382-014-2087-7, 2014.
- Zhang, X., Lohmann, G., Knorr, G. and Xu, X.: Different ocean states and transient characteristics in Last Glacial Maximum simulations and implications for deglaciation, *Clim Past*, 9(5), 2319–2333, doi:10.5194/cp-9-2319-2013, 2013.

**Änderungen und Kommentare des Hauptdokuments**

<b>Seite 3: Eingefügt</b>	<b>Martin Werner</b>	<b>11.12.15 14:34</b>
(e.g., Stenni et al., 2010; Vimeux et al., 1999)		
<b>Seite 3: Gelöscht</b>	<b>Martin Werner</b>	<b>11.12.15 14:55</b>
2013		
<b>Seite 3: Eingefügt</b>	<b>Martin Werner</b>	<b>11.12.15 14:55</b>
2012		
<b>Seite 3: Eingefügt</b>	<b>Martin Werner</b>	<b>09.12.15 16:47</b>
, changes to regional moisture sources and the intensity or provenance of atmospheric transport pathways (LeGrande and Schmidt, 2009; Dayem et al., 2010; Lewis et al., 2010; Maher and Thompson, 2012; Caley et al., 2014a; Tan, 2014)		
<b>Seite 3: Eingefügt</b>	<b>Martin Werner</b>	<b>11.12.15 14:22</b>
the reconstruction of		
<b>Seite 3: Gelöscht</b>	<b>Martin Werner</b>	<b>11.12.15 14:22</b>
reconstructing		
<b>Seite 3: Eingefügt</b>	<b>Martin Werner</b>	<b>09.12.15 16:56</b>
b		
<b>Seite 5: Eingefügt</b>	<b>Martin Werner</b>	<b>11.12.15 14:59</b>
Risi et al., 2013;		
<b>Seite 6: Eingefügt</b>	<b>Martin Werner</b>	<b>22.12.15 10:30</b>
As compared to an atmosphere-only or ocean-only setup, a fully coupled model with an explicit stable water isotope diagnostics will be physically much more consistent regarding relevant fractionation processes during ocean-atmosphere interactions. For past climates, such a coupled isotope model can also generate isotopic compositions in various water reservoirs (e.g. a deuterium excess distribution in ocean surface waters) that are unavailable from proxy data but required as prescribed boundary conditions for uncoupled atmosphere and ocean simulations.		
<b>Seite 7: Gelöscht</b>	<b>Martin Werner</b>	<b>11.12.15 09:54</b>
, defined as the period 23,000 - 19,000yrs before present,		
<b>Seite 7: Eingefügt</b>	<b>Martin Werner</b>	<b>11.12.15 09:54</b>
<b>Seite 8: Eingefügt</b>	<b>Martin Werner</b>	<b>22.12.15 09:49</b>



Furthermore, it might be relevant for paleoclimate records, where the isotope signal reflects changes in the soil water (e.g., speleothems, ancient groundwater), as a potential fractionation during evapotranspiration processes might lead to substantial changes in the  $\delta^{18}\text{O}$  and deuterium excess signal of soil water (Haese et al., 2013). However, it remains an open question if such changes would also affect the simulated glacial anomalies ( $\Delta_{\text{LGM-PI}} \delta^{18}\text{O}$ ,  $\Delta_{\text{LGM-PI}} \text{dex}$ ), or simply lead to an equivalent strong change of  $\delta^{18}\text{O}$  and deuterium excess for both the PI and LGM simulations (without any glacial change).

<b>Seite 11: Eingefügt</b>	<b>Martin Werner</b>	<b>16.12.15 08:16</b>
----------------------------	----------------------	-----------------------

5

<b>Seite 11: Gelöscht</b>	<b>Martin Werner</b>	<b>16.12.15 08:16</b>
---------------------------	----------------------	-----------------------

4

<b>Seite 11: Eingefügt</b>	<b>Martin Werner</b>	<b>22.12.15 08:23</b>
----------------------------	----------------------	-----------------------

. As in previous uncoupled studies (e.g. Risi et al., 2010; Werner et al., 2001) we assume no glacial change of the mean deuterium excess in the ocean, which implies a glacial change of  $\delta\text{D}$  of +8‰.

<b>Seite 11: Gelöscht</b>	<b>Martin Werner</b>	<b>22.12.15 08:52</b>
---------------------------	----------------------	-----------------------

( $\delta\text{D}$ : +8‰).

<b>Seite 11: Eingefügt</b>	<b>Martin Werner</b>	<b>16.12.15 08:16</b>
----------------------------	----------------------	-----------------------

5

<b>Seite 11: Gelöscht</b>	<b>Martin Werner</b>	<b>16.12.15 08:16</b>
---------------------------	----------------------	-----------------------

3

<b>Seite 12: Gelöscht</b>	<b>Martin Werner</b>	<b>11.12.15 15:03</b>
---------------------------	----------------------	-----------------------

is

<b>Seite 12: Eingefügt</b>	<b>Martin Werner</b>	<b>11.12.15 15:03</b>
----------------------------	----------------------	-----------------------

are

<b>Seite 13: Eingefügt</b>	<b>Martin Werner</b>	<b>15.12.15 11:24</b>
----------------------------	----------------------	-----------------------

of  $\delta^{18}\text{O}$  in precipitation

<b>Seite 13: Gelöscht</b>	<b>Martin Werner</b>	<b>16.12.15 13:02</b>
---------------------------	----------------------	-----------------------

we

<b>Seite 13: Eingefügt</b>	<b>Martin Werner</b>	<b>15.12.15 11:12</b>
----------------------------	----------------------	-----------------------

$\delta^{18}\text{O}$  values in calcite are converted between the PDB and SMOW scale as the following (Coplen, 1983; Sharp 2007):

$$\delta^{18}\text{O}_{\text{c(PDB)}} = 0.97002 * \delta^{18}\text{O}_{\text{c(SMOW)}} - 29.98$$

For an estimation of  $\delta^{18}\text{O}$  in the drip water we apply

<b>Seite 13: Gelöscht</b>	<b>Martin Werner</b>	<b>17.12.15 12:16</b>
---------------------------	----------------------	-----------------------

17

<b>Seite 13: Eingefügt</b>	<b>Martin Werner</b>	<b>17.12.15 12:16</b>
----------------------------	----------------------	-----------------------

42 + 0.27

<b>Seite 13: Eingefügt</b>	<b>Martin Werner</b>	<b>15.12.15 11:24</b>
----------------------------	----------------------	-----------------------

As mentioned above, we further assume that the  $\delta^{18}\text{O}$  values in drip water, calculate in such way, are a reliable proxy for the annual mean  $\delta^{18}\text{O}$  in precipitation falling at the cave site and can thus be directly compared to our model results.

<b>Seite 13: Gelöscht</b>	<b>Martin Werner</b>	<b>15.12.15 11:22</b>
---------------------------	----------------------	-----------------------

Conversion between  $\delta^{18}\text{O}$  values on PDB and SMOW scale is calculated as suggested by Coplen (1988):

$$\delta^{18}\text{O}_{\text{PDB}} = 0.97002 * \delta^{18}\text{O}_{\text{SMOW}} - 29.98$$

<b>Seite 13: Eingefügt</b>	<b>Martin Werner</b>	<b>09.12.15 16:56</b>
----------------------------	----------------------	-----------------------

b

<b>Seite 14: Eingefügt</b>	<b>Martin Werner</b>	<b>09.12.15 16:56</b>
----------------------------	----------------------	-----------------------

b

<b>Seite 14: Gelöscht</b>	<b>Martin Werner</b>	<b>17.12.15 11:51</b>
---------------------------	----------------------	-----------------------

SMOW

<b>Seite 14: Eingefügt</b>	<b>Martin Werner</b>	<b>17.12.15 11:51</b>
----------------------------	----------------------	-----------------------

PDB

<b>Seite 14: Gelöscht</b>	<b>Martin Werner</b>	<b>17.12.15 11:51</b>
---------------------------	----------------------	-----------------------

SMOW

<b>Seite 14: Eingefügt</b>	<b>Martin Werner</b>	<b>17.12.15 11:51</b>
----------------------------	----------------------	-----------------------

PDB

<b>Seite 14: Eingefügt</b>	<b>Martin Werner</b>	<b>15.12.15 15:50</b>
----------------------------	----------------------	-----------------------

The conversion between the PDB and SMOW isotope scales (can be expressed as  $\delta^{18}\text{O}_{\text{oce}}(\text{PDB}) = \delta^{18}\text{O}_{\text{oce}}(\text{VSMOW}) - 0.27$  (Hut, 1987).

<b>Seite 15: Eingefügt</b>	<b>Martin Werner</b>	<b>16.12.15 13:06</b>
----------------------------	----------------------	-----------------------

To convert the reported speleothem PI values of  $\delta^{18}\text{O}_{\text{c}}$  in calcite (Table 2) to  $\delta^{18}\text{O}_{\text{p}}$  in precipitated water, we apply the formulae given in section 3.3. For the required site temperatures, we have

interpolated annual mean ERA40 soil temperatures (layer #1, mean of the period 1961-1990) to the different speleothem sites.

Seite 15: Gelöscht	Martin Werner	16.12.15 13:47
GNIP		
Seite 15: Eingefügt	Martin Werner	16.12.15 13:47
observational		
Seite 15: Gelöscht	Martin Werner	16.12.15 13:48
67		
Seite 15: Eingefügt	Martin Werner	16.12.15 13:48
71		
Seite 16: Eingefügt	Martin Werner	21.12.15 12:37
1		
Seite 16: Gelöscht	Martin Werner	21.12.15 12:37
0		
Seite 16: Eingefügt	Martin Werner	21.12.15 12:37
0		
Seite 16: Gelöscht	Martin Werner	21.12.15 12:37
2		
Seite 16: Eingefügt	Martin Werner	21.12.15 12:37
5		
Seite 16: Gelöscht	Martin Werner	21.12.15 12:37
2		
Seite 16: Eingefügt	Martin Werner	21.12.15 12:38
3		
Seite 16: Gelöscht	Martin Werner	21.12.15 12:38
5		
Seite 16: Eingefügt	Martin Werner	21.12.15 12:38
2		
Seite 16: Gelöscht	Martin Werner	21.12.15 12:38
1		
Seite 16: Eingefügt	Martin Werner	21.12.15 12:38
5		

Seite 16: Gelöscht	Martin Werner	21.12.15 12:38
2		
Seite 17: Eingefügt	Martin Werner	15.12.15 10:09
, c		
Seite 17: Eingefügt	Martin Werner	15.12.15 10:09
, d		
Seite 17: Eingefügt	Martin Werner	15.12.15 10:10
(Fig. 4c)		
Seite 18: Eingefügt	Martin Werner	11.12.15 15:14
the		
Seite 18: Eingefügt	Martin Werner	11.12.15 15:14
flux		
Seite 18: Eingefügt	Martin Werner	11.12.15 15:15
The model results show some agreement to the predicted dex values in evaporation by Pfahl and Sodemann (2014) but i		
Seite 18: Gelöscht	Martin Werner	11.12.15 15:16
I		
Seite 18: Eingefügt	Martin Werner	11.12.15 15:17
further		
Seite 18: Eingefügt	Martin Werner	11.12.15 15:15
the		
Seite 18: Eingefügt	Martin Werner	11.12.15 15:15
flux		
Seite 19: Eingefügt	Martin Werner	22.12.15 14:27
The modelled slope between the simulated dex in vapour above the ocean surface and the related relative humidity rh (-6.3%/(10% rh change)) is very close to the value given by Merlivat and Jouzel (1979), though.		
Seite 19: Gelöscht	Martin Werner	22.12.15 14:33
This		
Seite 19: Eingefügt	Martin Werner	22.12.15 14:33
The		
Seite 20: Eingefügt	Martin Werner	21.12.15 13:19

4

Seite 20: Gelöscht	Martin Werner	21.12.15 13:19
--------------------	---------------	----------------

2

Seite 21: Eingefügt	Martin Werner	21.12.15 13:26
---------------------	---------------	----------------

6

Seite 21: Gelöscht	Martin Werner	21.12.15 13:26
--------------------	---------------	----------------

9

Seite 21: Eingefügt	Martin Werner	21.12.15 13:26
---------------------	---------------	----------------

7

Seite 21: Gelöscht	Martin Werner	21.12.15 13:26
--------------------	---------------	----------------

5

Seite 21: Eingefügt	Martin Werner	16.12.15 13:32
---------------------	---------------	----------------

For the ice core records, we compare the modelled change of  $\delta^{18}\text{O}_p$  in precipitation with the ice core data (Table 1).

Seite 21: Eingefügt	Martin Werner	16.12.15 13:18
---------------------	---------------	----------------

calculate the modelled change of  $\delta^{18}\text{O}_c$  in calcite, which is then

Seite 21: Eingefügt	Martin Werner	16.12.15 13:19
---------------------	---------------	----------------

d

Seite 21: Gelöscht	Martin Werner	16.12.15 13:19
--------------------	---------------	----------------

the model results

Seite 21: Eingefügt	Martin Werner	16.12.15 13:19
---------------------	---------------	----------------

(Table 2)

Seite 22: Eingefügt	Martin Werner	21.12.15 13:44
---------------------	---------------	----------------

7

Seite 22: Gelöscht	Martin Werner	21.12.15 13:44
--------------------	---------------	----------------

8

Seite 22: Gelöscht	Martin Werner	16.12.15 13:20
--------------------	---------------	----------------

p

Seite 22: Eingefügt	Martin Werner	21.12.15 13:45
---------------------	---------------	----------------

5

Seite 22: Gelöscht	Martin Werner	21.12.15 13:45
--------------------	---------------	----------------

4

Seite 22: Eingefügt	Martin Werner	21.12.15 14:31
8		
Seite 22: Gelöscht	Martin Werner	21.12.15 14:31
7		
Seite 22: Gelöscht	Martin Werner	21.12.15 14:31
198		
Seite 22: Eingefügt	Martin Werner	21.12.15 14:31
218		
Seite 22: Gelöscht	Martin Werner	21.12.15 14:32
80		
Seite 22: Eingefügt	Martin Werner	21.12.15 14:32
79		
Seite 22: Gelöscht	Martin Werner	16.12.15 15:32
3		
Seite 22: Eingefügt	Martin Werner	16.12.15 15:32
5		
Seite 22: Gelöscht	Martin Werner	16.12.15 15:32
5		
Seite 22: Eingefügt	Martin Werner	16.12.15 15:32
6		
Seite 22: Eingefügt	Martin Werner	21.12.15 14:36
4		
Seite 22: Gelöscht	Martin Werner	21.12.15 14:36
5		
Seite 23: Eingefügt	Martin Werner	09.12.15 16:56
b		
Seite 24: Eingefügt	Martin Werner	09.12.15 16:57
b		
Seite 24: Eingefügt	Martin Werner	09.12.15 16:57
b		
Seite 24: Eingefügt	Martin Werner	09.12.15 16:57
b		

<b>Seite 24: Eingefügt</b>	<b>Martin Werner</b>	<b>09.12.15 16:57</b>
----------------------------	----------------------	-----------------------

b

<b>Seite 25: Eingefügt</b>	<b>Martin Werner</b>	<b>22.12.15 09:06</b>
----------------------------	----------------------	-----------------------

As stated in Chapter 2, we assumed no glacial change of the mean deuterium excess signal in the glacial ocean. However, some recent data (Schrag et al., 2002) suggest a mean glacial dD increase of +7.2‰, which is slightly lower than the increase prescribed in our LGM simulation (+8‰). Such lower glacial dD increase would lead to a mean glacial change of the deuterium excess in ocean waters of -0.8‰. As a first-order estimate, such lowered deuterium excess signal in the ocean might lead to an equivalent lower deuterium excess value both in vapour above the ocean and, consequently, in precipitation, too.

<b>Seite 25: Gelöscht</b>	<b>Martin Werner</b>	<b>15.12.15 10:56</b>
---------------------------	----------------------	-----------------------

2

<b>Seite 25: Eingefügt</b>	<b>Martin Werner</b>	<b>15.12.15 10:56</b>
----------------------------	----------------------	-----------------------

1

<b>Seite 26: Eingefügt</b>	<b>Martin Werner</b>	<b>11.12.15 14:19</b>
----------------------------	----------------------	-----------------------

t

<b>Seite 26: Eingefügt</b>	<b>Martin Werner</b>	<b>22.12.15 10:11</b>
----------------------------	----------------------	-----------------------

Apart from glacial SST changes, changes in the source areas of water transported to Antarctica and Greenland, e.g. by a glacial change in sea ice coverage, might lead to the change in the deuterium excess signal in polar precipitation, too. The simulated sea ice coverage of the COSMOS LGM simulation has already been described in detail in Zhang et al. (2013) and our simulation results are comparable to this previous study. For the southern hemisphere, there is a reasonable agreement between the simulated sea ice concentration and proxy data by Gersonde et al. (2005), such as the austral winter sea ice extent in the Atlantic sector and the austral summer sea ice extent in the Indian ocean sector. However, the simulation might underestimate a larger extent of sporadic summer sea ice between 5°E and 5°W in the Southern Ocean, as discussed in Gersonde et al. (2005). As compared to the ECHAM5 experiment with GLAMAP data, a much-reduced sea ice cover in austral summer is found in this coupled ECHAM5/MPI-ESM LGM simulation. This reduction might lead to a stronger contribution of vapour stemming from regions between 60°-65°S to the Antarctic ice sheet. As vapour from these regions has a strong negative

deuterium excess signal (cf. Fig. 12) such shift in the source contributions might lead to a more negative deuterium excess signal in Antarctic precipitation, too.

**Seite 27: Eingefügt** **Martin Werner** **22.12.15 16:47**

These rather small variations of the LGM relative humidity changes are somewhat surprising, as cooler SST should lead to cooler air temperatures above the ocean surface, which then should lead to higher relative humidity levels (if the amount of water in the air stays constant). However, we find in our simulations that the air directly above the ocean surface cools slightly stronger during the LGM than the SST themselves. This leads to a reduced glacial evaporation flux from the ocean to the atmosphere, which decreases the relative humidity of the vapour and counterbalance the first effect. Similar small changes of relative humidity changes above the ocean surface and the counterbalance of different effects have recently been reported for a set of CMIP5 climate model results by Laîné et al. (2014). They have analysed a future warmer climate, though.

**Seite 27: Eingefügt** **Martin Werner** **22.12.15 13:29**

, the correlation between vapour dex and SST changes does not rule out other influencing factors, like wind speed changes, which might affect both the deuterium excess signal and SST changes, simultaneously. Furthermore,

**Seite 27: Gelöscht** **Martin Werner** **22.12.15 13:29**

**Seite 29: Gelöscht** **Martin Werner** **11.12.15 14:16**

CLIMAP

**Seite 29: Eingefügt** **Martin Werner** **11.12.15 14:16**

MARGO

**Seite 31: Eingefügt** **Martin Werner** **09.12.15 16:57**

Caley, T., Roche, D. M. and Renssen, H.: Orbital Asian summer monsoon dynamics revealed using an isotope-enabled global climate model, Nature Communications, 5, doi:10.1038/ncomms6371, 2014a.

**Seite 31: Eingefügt** **Martin Werner** **09.12.15 16:55**

b

**Seite 31: Gelöscht** **Martin Werner** **17.12.15 12:24**

Coplen, T. B.: Normalization of oxygen and hydrogen isotope data, Chem Geol, 72(4), 293–297, doi: 10.1016/0168-9622(88)90042-5, 1988.

**Seite 31: Eingefügt** **Martin Werner** **17.12.15 12:24**

Coplen, T. B., Kendall, C., and Hopple, J.: Comparison of stable isotope reference samples,



Nature, 302, 236–238, 1983.

<b>Seite 32: Eingefügt</b>	<b>Martin Werner</b>	<b>09.12.15 16:52</b>
Dayem, K. E., Molnar, P., Battisti, D. S. and Roe, G. H.: Lessons learned from oxygen isotopes in modern precipitation applied to interpretation of speleothem records of paleoclimate from eastern Asia, <i>Earth Planet. Sci. Lett.</i> , 295(1-2), 219–230, doi:10.1016/j.epsl.2010.04.003, 2010.		
<b>Seite 32: Eingefügt</b>	<b>Martin Werner</b>	<b>22.12.15 11:09</b>
Gersonde, R., Crosta, X., Abelmann, A. and Armand, L.: Sea-surface temperature and sea ice distribution of the Southern Ocean at the EPILOG Last Glacial Maximum - A circum-Antarctic view based on siliceous microfossil records, <i>Quaternary Sci Rev</i> , 24(7-9), 869–896, doi:10.1016/j.quascirev.2004.07.015, 2005.		
<b>Seite 33: Eingefügt</b>	<b>Martin Werner</b>	<b>15.12.15 16:01</b>
Hut, G.: Stable Isotope Reference Samples for Geochemical and Hydrological Investigations. Consultant Group Meeting IAEA, Vienna 16–18 September 1985, Report to the Director General, International Atomic Energy Agency, Vienna, 1987.		
<b>Seite 34: Eingefügt</b>	<b>Martin Werner</b>	<b>22.12.15 16:50</b>
Lainé, A., Nakamura, H., Nishii, K. and Miyasaka, T.: A diagnostic study of future evaporation changes projected in CMIP5 climate models, <i>Clim. Dyn.</i> , 42(9-10), 2745–2761, doi:10.1007/s00382-014-2087-7, 2014.		
<b>Seite 34: Eingefügt</b>	<b>Martin Werner</b>	<b>09.12.15 17:00</b>
Maher, B. A. and Thompson, R.: Oxygen isotopes from Chinese caves: records not of monsoon rainfall but of circulation regime, <i>J. Quat. Sci.</i> , 27(6), 615–624, doi:10.1002/jqs.2553, 2012.		
<b>Seite 35: Eingefügt</b>	<b>Martin Werner</b>	<b>11.12.15 15:02</b>
Risi, C., Landais, A., Winkler, R. and Vimeux, F.: Can we determine what controls the spatio-temporal distribution of d-excess and O-17-excess in precipitation using the LMDZ general circulation model? <i>Clim Past</i> , 9(5), 2173–2193, doi:10.5194/cp-9-2173-2013, 2013.		
<b>Seite 36: Eingefügt</b>	<b>Martin Werner</b>	<b>22.12.15 11:06</b>
Schrag, D. P., Adkins, J. F., McIntyre, K., Alexander, J. L., Hodell, D. A., Charles, C. D. and McManus, J. F.: The oxygen isotopic composition of seawater during the Last Glacial Maximum, <i>Quaternary Sci Rev</i> , 21(1-3), 331–342, doi:10.1016/S0277-3791(01)00110-X, 2002.		
<b>Seite 37: Eingefügt</b>	<b>Martin Werner</b>	<b>17.12.15 12:22</b>
Sharp, Z.: Principles of Stable Isotope Geochemistry, Pearson Prentice Hall, Upper Saddle River, New Jersey, 2007.		
<b>Seite 37: Eingefügt</b>	<b>Martin Werner</b>	<b>09.12.15 17:04</b>
Tan, M.: Circulation effect: response of precipitation delta O-18 to the ENSO cycle in monsoon regions of China, <i>Clim. Dyn.</i> , 42(3-4), 1067–1077, doi:10.1007/s00382-013-1732-x, 2014.		
<b>Seite 38: Eingefügt</b>	<b>Martin Werner</b>	<b>11.12.15 14:53</b>
Vimeux, F., Gallaire, R., Bony, S., Hoffmann, G. and Chiang, J.: What are the climate controls		

on  $\delta D$  in precipitation in the Zongo Valley (Bolivia)? Implications for the Illimani ice core interpretation, Earth Planet. Sci. Lett., 240(2), 205–220, doi:10.1016/j.epsl.2005.09.031, 2005.

<b>Seite 42: Eingefügt</b>	<b>Martin Werner</b>	<b>16.12.15 13:39</b>
21 ice core records		
<b>Seite 42: Gelöscht</b>	<b>Martin Werner</b>	<b>15.12.15 10:56</b>
8 speleothem records		
<b>Seite 42: Eingefügt</b>	<b>Martin Werner</b>	<b>15.12.15 10:56</b>
8 speleothem records		
<b>Seite 42: Gelöscht</b>	<b>Martin Werner</b>	<b>15.12.15 10:56</b>
16 ice core records		
<b>Seite 42: Gelöscht</b>	<b>Martin Werner</b>	<b>15.12.15 10:08</b>
Background pattern:		
<b>Seite 42: Eingefügt</b>	<b>Martin Werner</b>	<b>15.12.15 10:08</b>
for the same regions (Atlantic Ocean: n = 5811, Pacific Ocean: n = 2985)		
<b>Seite 42: Eingefügt</b>	<b>Martin Werner</b>	<b>15.12.15 10:08</b>
in panel (c) and (d)		
<b>Seite 42: Gelöscht</b>	<b>Martin Werner</b>	<b>22.12.15 16:55</b>
For improved readability, only an arbitrary subset of 300 data entries from the complete available GISS data set (Atlantic Ocean: n = 5811, Pacific Ocean: n = 2985) is shown in each panel.		
<b>Seite 43: Eingefügt</b>	<b>Martin Werner</b>	<b>16.12.15 13:37</b>
in precipitation		
<b>Seite 43: Eingefügt</b>	<b>Martin Werner</b>	<b>16.12.15 13:37</b>
in precipitation		
<b>Seite 43: Eingefügt</b>	<b>Martin Werner</b>	<b>16.12.15 13:38</b>
(Table 1)		
<b>Seite 43: Eingefügt</b>	<b>Martin Werner</b>	<b>16.12.15 13:38</b>
in calcite of		
<b>Seite 43: Gelöscht</b>	<b>Martin Werner</b>	<b>16.12.15 13:38</b>
in		
<b>Seite 43: Eingefügt</b>	<b>Martin Werner</b>	<b>16.12.15 13:38</b>
(Table 2)		
<b>Seite 44: Eingefügt</b>	<b>Martin Werner</b>	<b>09.12.15 16:57</b>

b

b

**Änderungen der Kopf- und Fußzeile**

**Textfeld-Änderungen**

**Änderungen an Textfeldern in der Kopf- und Fußzeile**

**Fußnoten-Änderungen**

**Endnoten-Änderungen**

1 **Glacial-interglacial changes of H<sub>2</sub><sup>18</sup>O, HDO and Deuterium**  
2 **Excess - results from the fully coupled Earth System Model**  
3 **ECHAM5/MPI-OM**

4 **M. Werner<sup>1</sup>, B. Haese<sup>1,2</sup>, X. Xu<sup>1,3</sup>, X. Zhang<sup>1</sup>, M. Butzin<sup>1</sup>, G. Lohmann<sup>1</sup>**  
5  
6

7 [1]{Alfred Wegener Institute, Helmholtz Centre for Polar and Marine Sciences, Bremerhaven,  
8 Germany}

9 [2]{Chair for Regional Climate and Hydrology, University of Augsburg, Germany}

10 [3]{Institute of Geosciences, Department of Geology, Kiel University, Germany}

11

12

13 Correspondence to:

14 Martin Werner  
15 Alfred Wegener Institute  
16 Helmholtz Centre for Polar and Marine Research  
17 Division Climate Science | Paleoclimate Dynamics  
18 Bussestr. 24  
19 D-27570 Bremerhaven  
20 Germany  
21 email: martin.werner@awi.de  
22

23 **Abstract**

24 In this study we present first results of a new isotope-enabled general circulation model setup.  
25 The model consists of a fully coupled atmosphere-ocean model ECHAM5/MPI-OM,  
26 enhanced by the interactive land surface scheme JSBACH and an explicit hydrological  
27 discharge scheme to close the global water budget. Stable water isotopes  $\text{H}_2^{18}\text{O}$  and HDO  
28 have been incorporated into all relevant model components. Results of two equilibrium  
29 simulations under pre-industrial and last glacial maximum conditions are analysed and  
30 compared to observational data and paleoclimate records for evaluating the model's  
31 performance of simulating spatial and temporal variations in the isotopic composition of the  
32 Earth's water cycle. For the pre-industrial climate, many aspects of the simulation results of  
33 meteoric waters are in good to very good agreement with both observations and earlier  
34 atmosphere-only simulations. The model is capable of adequately simulating the large spread  
35 in the isotopic composition of precipitation between low and high latitudes. A comparison to  
36 available ocean data also shows a good model-data agreement, however a strong bias of too  
37 depleted ocean surface waters is detected for the Arctic region. Simulation results under last  
38 glacial maximum boundary conditions also fit to the wealth of available isotope records from  
39 polar ice cores, speleothems, as well as marine calcite data. Data-model evaluation of the  
40 isotopic composition in precipitation reveals a good match of the model results and indicates  
41 that the temporal glacial-interglacial isotope-temperature relation was substantially lower than  
42 the present spatial gradient for most mid- to high-litudinal regions. As compared to older  
43 atmosphere-only simulations, a remarkable improvement is achieved for the modelling of the  
44 deuterium excess signal in Antarctic ice cores. Our simulation results indicate that cool sub-  
45 tropical and mid-litudinal sea surface temperatures are key for this progress. A recently  
46 discussed revised interpretation of the deuterium excess record of Antarctic ice cores in terms  
47 of marine relative humidity changes on glacial-interglacial timescales is not supported by our  
48 model results.

49

## 50 1 Introduction

51 The water cycle is a key component of the Earth's climate system. Documenting and  
52 understanding its past evolution is essential to test our ability to model its future changes.  
53 Water stable isotopes ( $\text{H}_2^{18}\text{O}$ ,  $\text{HD}^{16}\text{O}$ , and  $\text{H}_2^{17}\text{O}$ ) are integrated tracers of climate processes  
54 occurring in various branches of this cycle (Craig and Gordon, 1965; Dansgaard, 1964). They  
55 have been successfully used to describe past climate changes for more than 30 years. For  
56 example, water stable isotopes (hereafter expressed in a  $\delta$ -notation as  $\delta^{18}\text{O}$  and  $\delta\text{D}$ , with  
57 respect to the Vienna Standard Mean Ocean Water standard V-SMOW, if not stated  
58 otherwise) have been measured routinely over the past decades in polar ice cores (Jouzel,  
59 2013) and more recently also in non-polar ice cores (Hoffmann et al., 2003; Thompson et al.,  
60 1998). To a first order,  $\delta^{18}\text{O}$  and  $\delta\text{D}$  in polar ice cores are used for past temperature  
61 reconstructions over the past glacial-interglacial cycles (Jouzel et al., 2007; NEEM  
62 community members, 2013). In addition to high-resolution temperature records, the  
63 combination of water isotopic ratios permits to have a tracer of the low latitudes in polar ice  
64 cores ([e.g., Stenni et al., 2010; Vimeux et al., 1999](#)). For other (sub-)tropical isotope archives,  
65 e.g. speleothems, some studies have suggested are indicating that the amount of precipitation  
66 could be mainly responsible for determining the water isotope concentration (Fleitmann et al.,  
67 2003; Wang et al., 2001) – this is called the amount effect (Dansgaard, 1964; Rozanski et al.,  
68 1992). Furthermore, in these regions  $\delta^{18}\text{O}$  and  $\delta\text{D}$  might also reflect convective activity along  
69 moisture trajectory (Vimeux et al., 2005; Yao et al., ~~2013~~2012), [changes to regional moisture](#)  
70 [sources and the intensity or provenance of atmospheric transport pathways \(LeGrande and](#)  
71 [Schmidt, 2009; Dayem et al., 2010; Lewis et al., 2010; Maher and Thompson, 2012; Caley et](#)  
72 [al., 2014a; Tan, 2014\)](#). High resolution and well-dated records of  $\delta^{18}\text{O}$  of calcite in tropical  
73 speleothems in Asia or South America have therefore been interpreted in terms of past  
74 monsoon dynamics (Cruz et al., 2005; Wang et al., 2008). Analogously to continental  
75 speleothem archives, the seawater oxygen isotope concentration ( $\delta^{18}\text{O}_{\text{oce}}$ ) is conserved in  
76 carbonates ( $\delta^{18}\text{O}_{\text{c}}$ ) from corals, foraminifers, and other marine species. Here, temperature  
77 during calcite formation and the isotopic composition of the seawater  $\delta^{18}\text{O}_{\text{c}}$  are both the key  
78 factors controlling  $\delta^{18}\text{O}_{\text{c}}$  (Shackleton, 1974). Thus, carbonate isotope records from ocean  
79 sediment cores are fundamental records to access the water mass changes in a different  
80 climate. A considerable body of literature shows that they allow [the reconstruction of](#)  
81 ~~reconstructing~~ the three-dimensional structure of the ocean when the number of records is  
82 sufficient (Caley et al., 2014**b**; Roche et al., 2014).

83 As a second order isotope effect, the deuterium excess – defined as  $\text{dex} = \delta\text{D} - 8 \cdot \delta^{18}\text{O}$  – is a  
84 quantity, which primarily depends on climatic conditions during evaporative processes  
85 (Dansgaard, 1964). According to Merlivat and Jouzel (1979), key parameters that influence  
86 the dex signal of the evaporation flux from ocean surface are both relative humidity above the  
87 ocean surface as well as water temperature during evaporation. For many years, it has been  
88 assumed that relative humidity is remaining almost constant during climate changes and the  
89 dex signal of polar ice cores has been used to infer past sea surface temperature changes  
90 (Jouzel and Merlivat, 1984; Masson-Delmotte et al., 2005; Steen-Larsen et al., 2014b; Stenni  
91 et al., 2001; Vimeux et al., 1999). Recently, Pfahl and Sodemann (2014) have challenged this  
92 assumption by arguing that moisture source relative humidity, and not sea surface  
93 temperature, is the main driver of dex variability, at least on the present-day seasonal  
94 timescale. Their findings are based on the use of an empirical relation between dex and  
95 relative humidity together with ERA-Interim reanalysis data (Dee et al., 2011) to globally  
96 predict dex values of evaporation fluxes over the ocean. Their results are partly supported by  
97 recent monitoring studies of water vapour isotopic composition, which have demonstrated a  
98 strong imprint of source humidity in the North Atlantic on the high deuterium excess of  
99 Arctic water vapour (Bonne et al., 2014; Steen-Larsen et al., 2014b; 2013).

100 However, while direct or indirect records of water isotopes in natural archives provide key  
101 documentation of past climate variations, their quantitative translation to climate variables  
102 such as temperature or precipitation amount still remains uncertain in many cases. Since the  
103 beginning, the interpretation of isotopic time series has been almost entirely based on a  
104 modern analogue approach. It is assumed that the observed spatial or seasonal relationship  
105 between isotopes and surface temperatures, precipitation amount, or salinity provides a  
106 calibration, which is also valid for different climates of the past. This hypothesis was  
107 originally supported by the close relationship observed between modern annual mean  
108 precipitation isotope values and local annual mean temperature, precipitation amounts, or  
109 salinity, and for the atmosphere quantitatively it is consistent with a Rayleigh distillation  
110 process. However, this hypothesis is increasingly challenged (i) by new present-day  
111 observations, (ii) by alternative paleothermometry methods showing changing relationships  
112 for past periods (Buizert et al., 2014; Jouzel, 1999). This calls for a revised understanding of  
113 the interpretation of water stable isotopes, including second-order parameters such as  
114 deuterium excess, and their relationships with climatic conditions influencing the isotope  
115 signal.

116 One key tool for such an improved understanding of water isotopes in the Earth's  
117 hydrological cycle are atmospheric and oceanic general circulation models (GCM) with an  
118 explicit diagnostics of stable water isotopes. During the last three decades, several such  
119 isotope-enabled GCM have been built. Such models provide a mechanistic understanding of  
120 the physical processes influencing the isotopic composition of different water bodies in the  
121 climate system. They allow the explicit simulation of isotopic fractionation processes during  
122 any phase changes of a water mass within the model's hydrological cycle, e.g. during  
123 evaporation of water from land or ocean surface, cloud droplet formation, and re-evaporation  
124 of droplet water below cloud base. In such a isotope-enabled GCM setup, all relevant factors  
125 determining the strength and variability of isotopic fractionation are known.

126 The early implementations of water stable isotopes in atmospheric models (Hoffmann et al.,  
127 1998; Joussaume et al., 1984; Jouzel et al., 1987) have already shown their potential in  
128 explaining fundamental physical hydroclimate relationships. Since then, considerable  
129 progress has been made in simulating stable water isotopes in climate models, as the climate  
130 models have evolved themselves (Risi et al., 2010a; Werner et al., 2011). Using atmospheric  
131 models, water stable isotopes have been used for a considerable range of applications at small  
132 spatial and temporal scales such as investigating the link between water stable isotopes and  
133 decadal variability (Kurita et al., 2011) or to analyse mixing processes within rain events (Lee  
134 et al., 2009; Risi et al., 2010b). Many of these atmospheric GCM include at least two stable  
135 water isotopes (oxygen-18 and deuterium). With the improvements of the atmospheric GCM  
136 in simulating present-day water isotopic content, part of the interest has lately shifted to  
137 second order content such as deuterium excess and  $^{17}\text{O}$  excess that can provide further  
138 | constraints on the water cycle but remain challenging (Risi et al., 2010a; [Risi et al., 2013](#);  
139 Werner et al., 2011). Besides building atmospheric isotope-enabled GCM, several  
140 international groups have also worked on the inclusion of the water isotopes in oceanic GCM.  
141 Here, the water isotopic content is a passive tracer once the surface oceanic conditions are  
142 determined through the water balance with the atmosphere and the additional fractionation  
143 during sea-ice formation and melting. Attempts in oceanic-only GCM have proven useful to  
144 challenge the link between oceanic water isotopic content and salinity (Delaygue et al., 2000;  
145 Paul et al., 1999; Schmidt, 1998), a subject of considerable interest in paleoceanography.

146 In general, simulating evolving climate conditions requires using self-contained climate  
147 models as much as possible, to avoid prescribing unnecessary or unknown boundary



148 conditions. In particular for past climates applications, it is necessary to simulated stable  
149 water isotopes in the full water cycle system, not only in its atmospheric part. As compared to  
150 an atmosphere-only or ocean-only setup, a fully coupled model with an explicit stable water  
151 isotope diagnostics will be physically much more consistent regarding relevant fractionation  
152 processes during ocean-atmosphere interactions. For past climates, such a coupled isotope  
153 model can also generate isotopic compositions in various water reservoirs (e.g. a deuterium  
154 excess distribution in ocean surface waters) that are unavailable from proxy data but required  
155 as prescribed boundary conditions for uncoupled atmosphere and ocean simulations. So far  
156 however, few studies have used fully coupled isotope-enabled climate general circulation  
157 models to address questions related to the water cycle. Schmidt et al. (2007) incorporated  
158 water isotopes within the water cycle of the Goddard Institute for Space Studies (GISS)  
159 coupled ocean-atmosphere model (ModelE). In several multi-centennial simulations, they  
160 examined the internal variability and the simulated changes due to orbital and greenhouse gas  
161 forcing. Their study was restricted to the modern (preindustrial) and mid-Holocene (6kyrs  
162 B.P.) climates. LeGrande et al. (2009) expanded these analyses by performing eight Holocene  
163 time slice simulations, each ~1000 years apart. Lewis et al. (2010) used the same GISS-E  
164 model for simulating the consequences of a large freshwater input into the North Atlantic as  
165 an idealized analogue to iceberg discharge during Heinrich events. As a second fully coupled  
166 GCM, the HadCM3 model, has been enhanced by a stable water isotope diagnostics module  
167 by Tindall et al. (2009) for analyses of the present-day isotopic signature of El Niño–  
168 Southern Oscillation and the tropical amount effect. Besides these two fully coupled isotope-  
169 enabled GCM, there have also been some efforts in including water stable isotopes in the  
170 hydrological cycle of Earth System Models of Intermediate Complexity (EMICs) by Roche et  
171 al. (2004), Brennan et al. (2012), as well as Roche and Caley (2013). These isotope-enabled  
172 EMICs can be classified as an alternative tool to test ideas, explore large periods of time in a  
173 transient mode and guide much more computationally demanding simulations with fully  
174 coupled GCM.

175 The Paleoclimate Modeling Intercomparison Project (PMIP, <http://pmip3.lscce.ipsl.fr>) has  
176 chosen the Last Glacial Maximum (LGM) climate as one of the target periods for the  
177 evaluation of GCM modelling results. The LGM climate is not only very different from the  
178 present and/or pre-industrial climate, but this latest glacial epoch offers also a wealth of  
179 terrestrial, marine, and ice core proxy data for an in-depth model-data comparison. As many  
180 of these data sets are based on water stable isotopes (e.g., speleothem data, marine calcite

181 data, ice core records) several studies with isotope-enabled GCM have also chosen the LGM  
182 as a key period for an evaluation of modelled  $\delta^{18}\text{O}$  and  $\delta\text{D}$  values with different proxy data  
183 (Jouzel et al., 2000; Lee et al., 2008; Lewis et al., 2013; Risi et al., 2010a).

184 Here we present first results of a newly developed isotope-enhanced version of the fully  
185 coupled GCM ECHAM5/MPI-OM. The model amalgamates our previous efforts to include  
186 stable water isotope diagnostics within the atmosphere GCM ECHAM5 (Werner et al., 2011),  
187 the land surface scheme JSBACH (Haese et al., 2013), as well as the ocean GCM MPI-OM  
188 (Xu et al., 2012). Our following analysis and presentation of simulation results focus on the  
189 following questions: (a) How well does this fully-coupled Earth System Model simulate first-  
190 order isotopic variations ( $\delta^{18}\text{O}$ ,  $\delta\text{D}$ ) within different parts of the Earth's water cycle under pre-  
191 industrial and LGM, ~~defined as the period 23,000–19,000yrs before present,~~ boundary  
192 conditions? (b) Do the model results indicate substantial changes of the temperature-isotope  
193 relation of meteoric water? (c) Are simulated spatial and temporal variations of the deuterium  
194 excess in precipitation, a second-order isotope effect, also in agreement with available  
195 observations and paleoproxy data? (d) If so, how are these variations of deuterium excess  
196 related to past changes of evaporation processes?

## 197 **2 Model components and simulation setup**

### 198 **2.1 Model components**

199 In this study we use the Earth System Model ECHAM5/MPIOM, formerly also named as  
200 Community Earth System Model COSMOS. It is a fully coupled ocean-atmosphere-sea ice-  
201 land surface model (Jungclaus et al., 2006), which has now been enhanced by stable water  
202 diagnostics in all relevant model components. Previous studies with the standard (non-  
203 isotope) version of COSMOS have applied and evaluated this model, among others, for pre-  
204 industrial (Wei et al., 2012), glacial and interglacial climate states (Zhang et al., 2014; 2013),  
205 the Holocene (Wei and Lohmann, 2012) and Cenozoic climate change (Knorr et al., 2011;  
206 Stepanek and Lohmann, 2012).

207 During the recent years, all key model components (ECHAM5, MPI-OM, JSBACH) have  
208 been equipped with a diagnostic module to explicitly simulate both  $\text{H}_2^{18}\text{O}$  and HDO within  
209 the different parts of the hydrological cycle. Here, we give just a brief summary of key model

210 components and isotope implementation within them and refer to previous publications for  
211 details.

212 The atmosphere component of our model setup is the ECHAM5 atmosphere GCM, which has  
213 been mainly built at the Max Planck Institute for Meteorology, Hamburg. The model has a  
214 spectral, dynamical core, which is constrained by the equations of state describing the  
215 conservation of mass, energy, and momentum. Further model constraints are set by the  
216 continuity equation, a prediction equation for the surface pressure, as well as the hydrostatic  
217 equation (Roeckner et al., 2003). The water cycle in ECHAM5 contains formulations for  
218 evapotranspiration of terrestrial water, evaporation of ocean water, and the formation of large-  
219 scale and convective clouds. Within the atmosphere's advection scheme, vapour, liquid and  
220 frozen water are transported independently. A detailed model description is given in Roeckner  
221 et al. (2003; 2006). Stable water isotopes have been implemented into ECHAM5 in an  
222 analogous manner to previous ECHAM model releases (Hoffmann et al., 1998; Werner and  
223 Heimann, 2002). The isotope module in ECHAM5 computes the isotopic signal of different  
224 water masses within the entire water cycle. Details of the implementation have been reported  
225 in Werner et al. (2011). In the atmosphere-ocean coupled setup, ECHAM5 provides the  
226 required freshwater flux (P-E) and its isotopic composition for all ocean grid cells to the  
227 ocean model MPI-OM.

228 Within the ECHAM5 model setup used in this study, the JSBACH land surface model  
229 calculates the boundary conditions for ECHAM5 over terrestrial areas. This includes the  
230 exchange of water, energy, and momentum between the land surface and the atmosphere  
231 (Raddatz et al., 2007). JSBACH divides each land surface grid cell into 8 tiles covered by  
232 different plant functional types and bare soil. The simulated dynamical vegetation changes are  
233 controlled by the processes of natural growing and mortality, as well as disturbance mortality  
234 (e.g., wind, fire). Details of this approach are described in Brovkin et al. (2009). The water  
235 isotopes  $\text{H}_2^{18}\text{O}$  and HDO are almost passive tracers in the JSBACH model. No fractionation  
236 of the isotopes is assumed during most physical processes partitioning water masses on the  
237 land surface (e.g., snow melt, formation of surface water runoff and drainage; see Haese et al.,  
238 2013 for details). For evapotranspiration, fractionation of isotopes might occur during  
239 evaporation of water from bare soils. However, the strength of this fractionation remains an  
240 open question. In accordance with the results of Haese et al. (2013), we assume in this study  
241 that we can ignore any possible fractionation during evapotranspiration processes from

242 terrestrial areas, as our analyses will focus primarily on the isotopic composition of  
243 precipitation. This choice might add a small bias to the isotopic composition of terrestrial  
244 surface water pools and the discharge of terrestrial net precipitation (P–E) towards the oceans.  
245 Furthermore, it might be relevant for paleoclimate records, where the isotope signal reflects  
246 changes in the soil water (e.g., speleothems, ancient groundwater), as a potential fractionation  
247 during evapotranspiration processes might lead to substantial changes in the  $\delta^{18}\text{O}$  and  
248 deuterium excess signal of soil water (Haese et al., 2013). However, it remains an open  
249 question if such changes would also affect the simulated glacial anomalies ( $\Delta_{\text{LGM-PI}} \delta^{18}\text{O}$ ,  
250  $\Delta_{\text{LGM-PI}} \text{dex}$ ), or simply lead to an equivalent strong change of  $\delta^{18}\text{O}$  and deuterium excess for  
251 both the PI and LGM simulations (without any glacial change).

252 In the used coupled model setup, terrestrial water discharge to the ocean is calculated by the  
253 so-called Hydrological Discharge scheme (HD scheme; Hagemann and Gates, 2003).  
254 Modelled discharge is calculated with respect to the slope of the topography. For the  
255 simulated total river runoff it is assumed that the global water cycle is closed, i.e., all net  
256 precipitation (P-E) over terrestrial areas is transported to the ocean. However, lakes are absent  
257 in the HD scheme. This may lead to minor errors in the magnitude and location of the  
258 modelled river runoff compared to observations. As the ECHAM5/MPI-OM coupled model  
259 setup does not include a dynamic ice sheet model, precipitation amounts falling on glaciers  
260 are instantaneously put as runoff into to the nearest ocean grid cell for closing the global  
261 water budget. Independent of the chosen spatial ECHAM5 model resolution, the HD scheme  
262 is always implemented on a fine horizontal  $0.5^\circ \times 0.5^\circ$  degree grid and allows simulating water  
263 mass flows of the major river systems of the Earth. Stable water isotopes  $\text{H}_2^{18}\text{O}$  and HDO are  
264 incorporated as passive tracers within the HD scheme.

265 The ocean component of our model setup consists of the general circulation model MPIOM  
266 (Marsland et al., 2003), which is employed on a curvilinear Arakawa-C grid. The used  
267 MPIOM setup has a free surface and contains subgrid-scale parameterizations for convection,  
268 vertical and isopycnal diffusivity, horizontal and vertical viscosity, as well as for the bottom  
269 boundary layer flow across steep topography. Sea ice is simulated by a viscous-plastic  
270 rheology model (Hibler, 1979). It considers thermodynamic sea ice melt and growth, and also  
271 a thermohaline coupling by brine rejection. Stable water isotopes Within MPI-OM,  $\text{H}_2^{18}\text{O}$  and  
272 HDO are treated as passive tracers. They are fully mixed and advected within the model, and  
273 their total mass is conserved. Isotopic variations occur mainly due to temperature-dependent

274 isotope fractionation during evaporation, as well as by advection and mixing of different  
275 water masses. Changes of the oceanic water masses by terrestrial freshwater fluxes entering  
276 the ocean are included in the model setup, too. For the process of sea ice formation from  
277 liquid waters, the isotopic composition of sea ice is calculated by a liquid to ice equilibrium  
278 fractionation factor of 1.003, which is the average from various estimates (Craig and Gordon,  
279 1965; Lehmann and Siegenthaler, 1991; Macdonald et al., 1995; Majoube, 1971). Due to the  
280 very low rate of isotopic diffusion in sea ice, we assume no fractionation during sea ice  
281 melting. In the atmosphere-ocean coupled setup, MPI-OM provides the isotope composition  
282 of sea surface water and sea ice as a temporally varying boundary condition to the atmosphere  
283 model ECHAM5.

284 Within ECHAM5/MPI-OM, atmosphere and ocean are coupled via the Ocean-Atmosphere-  
285 Sea Ice-Soil OASIS3 coupler (Valcke et al., 2003). Mass, energy, and momentum fluxes, as  
286 well as the related isotope masses of H<sub>2</sub><sup>18</sup>O and HDO, are exchanged between the atmosphere  
287 and ocean once per day. The coupling is described in detail in Jungclaus et al. (2006).

## 288 **2.2 Simulation setup**

289 We have used the following simulation setup for all simulation results presented in this study:  
290 The atmospheric component ECHAM5 runs at a horizontal resolution of approx. 3.75°×3.75°  
291 with 19 vertical levels between surface and 10hPa (T31L19 resolution). The same horizontal  
292 resolution is applied for the land surface scheme JSBACH. The ocean model MPI-OM has a  
293 formal horizontal resolution of approx. 3°×1.8° and 40 uneven vertical layers on z-levels. The  
294 used MPI-OM model setup has a bipolar orthogonal spherical coordinate system, where the  
295 poles are placed over Greenland and Antarctica, respectively. Placing one pole over  
296 Greenland avoids a grid singularity in the Arctic Ocean. Furthermore, it ensures a high  
297 horizontal grid resolution in the deep-water formation regions of the northern North Atlantic  
298 Ocean and the Arctic.

299 Two different simulations were performed, one for the pre-industrial and one for the LGM  
300 climate. We briefly describe here these experimental setups: For the pre-industrial (PI)  
301 climate, ECHAM5/MPI-OM has been continued from a PI simulation without isotopes  
302 included, which has been in run into equilibrium over several thousand years (Wei et al.,  
303 2012; Zhang et al., 2013) using identical PI boundary conditions. At model start, isotope  
304 values in the atmosphere have been set to constant values ( $\delta^{18}\text{O}$ : -10‰,  $\delta\text{D}$ : -80‰), while the

305 oceanic isotope distribution has been taken from an equilibrium run over 3,000 years with the  
306 MPI-OM-wiso ocean model (Xu, 2012) with global mean  $\delta^{18}\text{O}$  and  $\delta\text{D}$  values of 0‰, each  
307 (Baertschi, 1976; de Wit et al., 1980). The fully coupled ECHAM5/MPI-OM model with  
308 included isotope diagnostics has then been run under PI boundary conditions (orbital forcing,  
309 greenhouse gas concentrations, ocean bathymetry, land surface and ice sheet topography) for  
310 another 1,5400 years. For the LGM simulation, we impose orbital forcing and greenhouse gas  
311 concentrations ( $\text{CO}_2 = 185$  ppm;  $\text{N}_2\text{O} = 200$  ppb;  $\text{CH}_4 = 350$  ppb) as well as surface boundary  
312 conditions (terrestrial topography, ocean bathymetry, runoff routes according ice sheet  
313 reconstruction) in accordance with the PMIP3 protocol (<http://pmip3.lsce.ipsl.fr/>). An  
314 increased global salinity (1 PSU added compared to modern values) accounts for a LGM sea  
315 level drop of approx. 116m. Again, the isotope-enabled version of ECHAM5/MPI-OM has  
316 been restarted from an already equilibrated simulation without isotopes (Zhang et al., 2013).  
317 The initial LGM oceanic  $\text{H}_2^{18}\text{O}$  and HDO distribution has been taken from a 3,000yrs long  
318 MPI-OM-wiso integration under LGM boundary conditions (Xu, 2012) with a prescribed  
319 glacial increase of  $\delta^{18}\text{O}$  of +1‰. As in previous uncoupled studies (e.g. Risi et al., 2010;  
320 Werner et al., 2001) we assume no glacial change of the mean deuterium excess in the ocean,  
321 which implies a glacial change of  $\delta\text{D}$  of +8‰. ~~( $\delta\text{D}$ : +8‰).~~ The fully coupled  
322 ECHAM5/MPI-OM model with included isotope diagnostics has then been run for another  
323 1,5300yrs.

324 At the end of the PI and LGM simulation period, none of the two runs shows any trend in the  
325 isotopic composition of ocean surface waters, and  $\delta^{18}\text{O}$  ( $\delta\text{D}$ ) trends in deep ocean waters at  
326 2200m are smaller than 0.005‰/100yrs (0.05‰/100yrs). Thus, we rate both simulations as  
327 equilibrated and consider the last 100 model years for our analyses.

328 If not stated otherwise, all reported  $\delta$  values of meteoric waters (precipitation, evaporation) in  
329 this study are calculated as precipitation (or evaporation)-weighted averages with respect to  
330 the V-SMOW scale. The  $\delta$ -values of ocean waters are calculated as arithmetic averages with  
331 respect to the V-SMOW scale.

### 332 **3 Observational data**

#### 333 **3.1 GNIP and GISS database**

334 The Global Network of Isotopes in Precipitation (GNIP) was initiated in 1958 by IAEA and  
335 WMO, and became operational in 1961 (IAEA/WMO, 2010). Since then, monthly samples of  
336  $\text{H}_2^{18}\text{O}$  and HDO in precipitation have been sampled at more than 900 stations from more than  
337 100 different countries. While several stations have continuously collected samples for two or  
338 more decades (e.g., GNIP stations in Krakow, Ottawa, Reykjavik, and Vienna), many other  
339 GNIP stations have been in operation for a much shorter period, only. Here, we use a subset  
340 of 70 stations from the GNIP database, where surface temperature, precipitation,  $\delta^{18}\text{O}$ , and  $\delta\text{D}$   
341 have been reported for a minimum of 5 calendar years, any time within the period 1961 to  
342 2007.

343 The GISS global seawater oxygen-18 database (Schmidt et al., 1999) is a collection of over  
344 26,000 seawater O-18 values made since about 1950. Partial versions of this database already  
345 appeared in Schmidt (1999) and Bigg and Rohling (2000). From this database we are using  
346 only values with no applied correction (see Schmidt et al., 1999 for details of the applied  
347 corrections). It is important to note that, in contrast to GNIP  $\delta^{18}\text{O}$  values of precipitation,  
348 GISS  $\delta^{18}\text{O}$  values in ocean water do not represent annual mean values, but are typically  
349 measured from a sample taken during an arbitrary day of the year. Therefore, we compare in  
350 this study the GISS data not to simulated annual mean isotope values in ocean waters, but to  
351 the long-term mean monthly value of the specific month, when a GISS  $\delta^{18}\text{O}$  value was  
352 reported.

#### 353 **3.2 Ice core data**

354 In the late 1960s Dansgaard (1969), Lorius (1979) and others started their pioneering work of  
355 analysing polar ice cores for climate research. Since then, the isotopic composition of more  
356 than a dozen deep ice cores both from Greenland and Antarctica has been measured. In  
357 parallel, alpine ice cores from (sub)tropical regions of South America (Hoffmann et al., 2003;  
358 Thompson et al., 1995), Africa (Thompson et al., 2002), and the Tibetan Plateau (Thompson  
359 et al., 1989; Tian et al., 2003; Yao et al., 2012) have been drilled and analysed during the last  
360 decades, too. In this study we use a subset of 6 Greenland, 10 Antarctic, and 5 (sub)tropical  
361 ice cores to compare the measured  $\delta^{18}\text{O}$  and  $\delta\text{D}$  values for the pre-industrial climate and the

362 LGM with our simulation results. For the different ice core records, we take the minimum  
363  $\delta^{18}\text{O}$  ( $\delta\text{D}$ , dex) value of the time interval 19,000 to 23,000 B.P. as a representative mean LGM  
364  $\delta^{18}\text{O}$  ( $\delta\text{D}$ , dex) value. The ice core data used in this study ~~is~~ are summarized in Table 1.

### 365 3.3 Speleothem calcite data

366 Recently, Shah et al. (2013) have published a global synthesis of speleothem  $\delta^{18}\text{O}$  records  
367 spanning the period from the LGM until present, which consists of data from 60 speleothems  
368 of 36 different sites. From this compilation we have selected a subset of 8 speleothem records  
369 (Table 2), where 1,000yrs-averaged  $\delta^{18}\text{O}$  values calculated by Shah et al. are available for  
370 both the LGM (defined here as period 19,000 to 22,000yrs B.P.) and the most recent 1,000yrs  
371 B.P. We use the latter as representative mean PI  $\delta^{18}\text{O}$  values at the different locations. We are  
372 aware that during the last 1,000 years B.P. the climate at a specific speleothem site might  
373 have been variable and different from the pre-industrial climate of our ECHAM5/MPI-OM  
374 simulation, which could lead to a bias in the model-data comparison. We are also aware that  
375 drip water in a cave, which isotopic composition is archived in a speleothem record, might be  
376 seasonally biased due to re-evaporation of the precipitated water (Wackerbarth et al., 2010).  
377 Furthermore, for many speleothems an additional fractionation between the drip water and the  
378 formed calcite can be observed (Dreybrodt and Scholz, 2011). Thus, necessary caution will be  
379 taken for the comparison of model results of  $\delta^{18}\text{O}$  in precipitation with the selected  
380 speleothem data.

381 All listed  $\delta^{18}\text{O}$  data in Table 2 are measured isotope values in carbonate and refer to the Pee  
382 Dee Belemnite (PDB) standard. For comparison with model results, ~~we~~  $\delta^{18}\text{O}$  values in calcite  
383 are converted between the PDB and SMOW scale as the following (Coplen, 1983; Sharp  
384 2007):

$$385 \quad \delta^{18}\text{O}_{\text{c(PDB)}} = 0.97002 * \delta^{18}\text{O}_{\text{c(SMOW)}} - 29.98$$

386 For an estimation of  $\delta^{18}\text{O}$  in the drip water we apply a formula linking  $\delta^{18}\text{O}$  in water and  $\delta^{18}\text{O}$   
387 in speleothem calcite, derived by Kim and O'Neil (1997) for synthetic calcite:

$$388 \quad \delta^{18}\text{O}_{\text{c(SMOW)}} = \delta^{18}\text{O}_{\text{water(SMOW)}} + 18.03 * (1000/T) - 32.1742 + 0.27$$

389 with T being the temperature (in Kelvin) during calcite formation. As mentioned above, we  
390 further assume that the  $\delta^{18}\text{O}$  values in drip water, calculate in such way, are a reliable proxy  
391 for the annual mean  $\delta^{18}\text{O}$  in precipitation falling at the cave site and can thus be directly



392 | ~~compared to our model results. Conversion between  $\delta^{18}\text{O}$  values on PDB and SMOW scale is~~  
393 | ~~calculated as suggested by Coplen (1988):~~  
394 |  ~~$\delta^{18}\text{O}_{\text{PDB}} = 0.97002 * \delta^{18}\text{O}_{\text{SMOW}} - 29.98$~~

### 395 | **3.4 Marine calcite data**

396 | Caley et al. (2014**b**) have recently compiled and published a marine calcite  $\delta^{18}\text{O}$  data set from  
397 | 114 (115) pairs of deep-sea cores, which contain both LGM and late Holocene planktic  
398 | (benthic) foraminifera  $\delta^{18}\text{O}$  data. In their study they report  $\delta^{18}\text{O}$  anomalies as the change  
399 | between mean  $\delta^{18}\text{O}$  values of the period 19,000 to 23,000yrs B.P. and over the last 3,000  
400 | years of each record. The MARGO project definition has been used to assure  
401 | chronostratigraphic quality of the selected data (Kucera et al., 2005). Planktic foraminifera  
402 | data have been mainly measured in the following species: *Globigerinoides sacculifer*,  
403 | *Globigerinoides ruber pink and white*, *Neogloboquadrina pachyderma sinistral*, and  
404 | *Globigerina bulloides*. Benthic foraminifera data includes, among others, *Cibicidoides*  
405 | *wuellerstorfi*, *Cibicidoides pachyderma*, and *Cibicidoides peregrina*. For a more detailed  
406 | description of this data set we refer to Caley et al. (2014**b**).

407 | According to Shackleton (1974) the  $\delta^{18}\text{O}_c$  signal in calcite shells of planktic and benthic  
408 | foraminifera can be interpreted by the following expression relating temperature to the  
409 | equilibrium fractionation of inorganic calcite precipitation around 16.9°C:

$$410 | T = 16.9 - 4.38 * (\delta^{18}\text{O}_{c(\text{PDB})} - \delta^{18}\text{O}_{\text{oce}(\text{SMOWPDB})}) + 0.1 * (\delta^{18}\text{O}_{c(\text{PDB})} - \delta^{18}\text{O}_{\text{oce}(\text{SMOWPDB})})^2$$

411 | with T being the temperature during calcite formation,  $\delta^{18}\text{O}_{c(\text{PDB})}$  the isotopic composition of  
412 | calcite on the PDB scale, and  $\delta^{18}\text{O}_{\text{oce}(\text{SMOW})}$  the isotopic composition of seawater on the  
413 | SMOW scale. The conversion between the PDB and SMOW isotope scales (can be expressed  
414 | as  $\delta^{18}\text{O}_{\text{oce}(\text{PDB})} = \delta^{18}\text{O}_{\text{oce}(\text{VSMOW})} - 0.27$  (Hut, 1987).

## 415 | **4 Results and discussion**

### 416 | **4.1 Present-day model evaluation**

#### 417 | **4.1.1 Isotopes in precipitation**

418 | Figure 1a shows the global distribution of annual mean  $\delta^{18}\text{O}$  values in precipitation ( $\delta^{18}\text{O}_p$ ) as  
419 | simulated by the ECHAM5/MPI-OM model with isotope diagnostics included. As for a

420 comparable simulation with the atmosphere-only model ECHAM5-wiso (Werner et al.,  
421 2011), all major characteristics of the global  $\text{H}_2^{18}\text{O}$  distribution in precipitation as previously  
422 reported by Dansgaard (1964) can be found in the global map of  $\delta^{18}\text{O}_p$ . In general, depletion  
423 of  $\delta^{18}\text{O}_p$  is in mid- to high-latitude regions as compared to values in the low latitudes  
424 (temperature effect). Strongest depletion of  $\delta^{18}\text{O}_p$  (down to -54‰) occurs over the polar ice  
425 sheets of Antarctica and Greenland. A longitudinal gradient of isotopic depletion in  
426 precipitation is simulated from the Atlantic Ocean towards Europe and Eurasia and towards  
427 eastern North America (continental effect). Strongly depleted  $\delta^{18}\text{O}_p$  values are also found over  
428 alpine mountain regions like the Andes and the Tibetan Plateau (altitude effect).

429 For a more quantitative evaluation of the model results, we compare the simulated annual  
430 mean  $\delta^{18}\text{O}_p$  values with observational data from the selected 70 GNIP stations, 21 ice cores,  
431 and 8 speleothems (Chapter 3). To convert the reported speleothem PI values of  $\delta^{18}\text{O}_c$  in  
432 calcite (Table 2) to  $\delta^{18}\text{O}_p$  in precipitated water, we apply the formulae given in section 3.3.  
433 For the required site temperatures, we have interpolated annual mean ERA40 soil  
434 temperatures (layer #1, mean of the period 1961-1990) to the different speleothem sites. We  
435 find that the modeled  $\delta^{18}\text{O}_p$  values are in good agreement with the ~~GNIP-observational~~ data,  
436 with a linear correlation coefficient  $r^2$  of 0.97, and a root mean square error (RMSE) of 3.0‰  
437 between measured and modelled  $\delta^{18}\text{O}_p$  values (Fig. 1b). For an evaluation of the modelled  
438 temperature effect (Fig. 1c) we focus on the ~~67-71~~ data sets in mid- to high-latitudinal regions  
439 with a annual mean temperature value below 20°C. The modelled global  $\delta^{18}\text{O}$  -T-gradient  
440 (0.58‰/°C;  $r^2 = 0.96$ ) is close to the observed gradient (0.66‰/°C;  $r^2 = 0.95$ ), with main  
441 deviations caused by an underestimation of depletion for cold regions with mean temperatures  
442 below -20°C. This result is similar to the findings for the ECHAM5-wiso atmosphere model,  
443 and the deviations can partly be explained by the coarse T31L19 model resolution (Werner et  
444 al., 2011). Similar distributions of  $\delta^{18}\text{O}$  and  $\delta\text{D}$  in precipitation have been reported for several  
445 atmosphere-only and fully coupled GCM during the last years (e.g., Lee et al., 2007; Risi et  
446 al., 2010a; Schmidt et al., 2007; Tindall et al., 2009). While all these models show a  
447 reasonable resemblance to GNIP observations for the large-scale patterns in low- and mid-  
448 latitudinal regions, some models have difficulties to correctly simulate the very low  
449 temperatures and strong isotope depletions over the Antarctic ice sheet (e.g., Lee et al., 2007).

#### 450 **4.1.2 Isotopes in ocean waters**

451 In Fig. 2a, the simulated annual mean  $\delta^{18}\text{O}_{\text{oce}}$  signal in ocean surface waters (mean over the  
452 depth interval between surface and 10m) are plotted. Mean values in the tropical to mid-  
453 latitudinal oceans range between +0.05‰ to +1.2‰, with a tendency to higher values in the  
454 Atlantic Ocean as compared to the Pacific and Indian Ocean. This relative enrichment can be  
455 explained by a net freshwater export of Atlantic Ocean water, which is transported westwards  
456 to the Pacific (Broecker et al., 1990; Lohmann, 2003; Zaucker and Broecker, 1992). The  
457 highest enrichment in the Atlantic Ocean is found south of Bermuda Island with surface water  
458  $\delta^{18}\text{O}_{\text{oce}}$  values of up to +1.3‰. Other, more localized regions of surface water  $\delta^{18}\text{O}_{\text{oce}}$   
459 enrichment with a similar order of magnitude are the Mediterranean Sea, the Black Sea, as  
460 well as the Red Sea. Again, this enrichment is most likely caused by a regional surplus of  
461 evaporation versus precipitation in these three regions. Stronger than average depletion of  
462  $\delta^{18}\text{O}_{\text{oce}}$  surface waters is simulated for both high-latitude ocean regions. While surface  
463 waters in the Southern Ocean between 50°S-75°S show a depletion of down to -0.8‰,  
464 modelled surface waters in the Arctic Ocean are depleted by down to -1.6‰. This depletion is  
465 most likely caused by two effects: (a) the implemented fractionation during sea ice formation  
466 which leads to an enrichment (depletion) of the isotopes in sea ice (the remaining liquid  
467 water); (b) the inflow of highly depleted water masses of Arctic rivers in combination with a  
468 strong stratification of the simulated Arctic Ocean water masses (see below).

469 For a quantitative evaluation of the model results, we compare the simulated values to 3859  
470  $\delta^{18}\text{O}$  entries of the selected GISS data (Chapter 3.1), which represent surface ocean water  
471 values between surface and 10m depth. On a global scale, the simulated  $\delta^{18}\text{O}_{\text{oce}}$  values agree  
472 quite well within a range of  $\pm 0.25\%$  with the GISS values (Fig. 2b). Strongest model-data  
473 deviations are found in the following regions: (a) In the vicinity of several large river  
474 estuaries the model results reveal too high  $\delta^{18}\text{O}_{\text{oce}}$  values (e.g., at the Amazon and Ganges  
475 river mouths); (b) the model also overestimates  $\delta^{18}\text{O}_{\text{oce}}$  in surface water in the Baltic Sea as  
476 well as in the Black Sea; (c) for the Arctic Ocean region the comparison yields mixed results:  
477 While the MPI-OM model tends to overestimate  $\delta^{18}\text{O}_{\text{oce}}$  in ocean surface waters in some  
478 regions by more than +2‰ (e.g. the eastern coast of Greenland, and in the Beaufort Sea north  
479 of Alaska), in most other Arctic regions the model results are lower by more than -2‰ than  
480 the GISS observations (e.g., in the Hudson Bay area, and the Barents Sea, the Kara Sea, as  
481 well as the Laptev Sea).

482 A separation of the model-data comparison into Atlantic, Pacific, Indian, and Arctic Ocean,  
483 does not show any systematic deviations between modelled  $\delta^{18}\text{O}_{\text{oce}}$  values and the GISS data  
484 for the first three oceans (Fig. 3). We find strong correlations between modelled values and  
485 the GISS data as well as a RMSE below 1‰ for all 3 oceans (Atlantic:  $n = 458$ ,  $r^2 = 0.919$ ,  
486 RMSE = 0.77; Pacific:  $n = 736$ ,  $r^2 = 0.602$ , RMSE = 0.752, Indian Ocean:  $n = 345$ ,  $r^2 = 0.46$ ,  
487 RMSE = 0.46). The strongest deviations of model values from observational data are caused  
488 by the overestimation of  $\delta^{18}\text{O}_{\text{oce}}$  values near river estuaries, at the Baltic Sea, and at the Sea of  
489 Okhotsk. For the Arctic Ocean, the majority of the simulated  $\delta^{18}\text{O}_{\text{oce}}$  values is stronger  
490 depleted than the corresponding GISS entries and the model-data correlation is worse ( $n =$   
491  $410$ ,  $r^2 = 0.335$ , RMSE = 2.2152). This bias in our ECHAM5/MPI-OM model is most likely  
492 caused by a too stratified Arctic Ocean. Highly depleted water inflowing from Arctic rivers  
493 remains in the upper layers of the Arctic Ocean and is not well mixed with deeper waters.  
494 This model deficit is clearly depicted in a comparison of the mean modelled isotope signal  
495 with available measurements from the GISS database in meridional sections of the Atlantic  
496 (zonal mean between 60°W-0°W; Fig. 4a, c) and the Pacific basin (zonal mean of region  
497 150°E to 110°W; Fig. 4b, d). For both cross sections, we find that the overestimated depletion  
498 of  $\delta^{18}\text{O}_{\text{oce}}$  values in the Arctic reaches down to approx. 500m below the surface while  
499 simulated North Atlantic Deep Water (NADW) masses are less depleted and in better  
500 agreement with the GISS data. Similar low isotope values in the Arctic oceans have already  
501 been reported by former studies with ocean-only GCM (Paul et al., 1999; Xu et al., 2012).

502 In general, we find for the Atlantic Ocean a fair agreement between GISS observations and  
503 model values. The regions of the strongest enrichment is located between 40°S to 30°N, with  
504 maximum enrichment (+0.6‰ or more) at approx. 20°S and 30°N, and a decreasing trend of  
505 enrichment in deeper water until approx. +0.1‰ at a depth of 3,000m. The enriched water  
506 masses are also found in NADW below 1,000m, with an enrichment of up to +0.2‰ (Fig. 4a).  
507 On the contrary, Atlantic water masses south of 40°S show a relative depletion down to -  
508 0.4‰ in their isotopic signature for all water depth, in agreement with available GISS data  
509 (Fig. 4c). Depleted water masses stemming from the Antarctic Bottom Water (AABW) are  
510 reaching until the equator where the isotopic signal is then mixed with NADW and enriched  
511 tropical Atlantic waters. For the Pacific (Fig. 4b) we find a similar vertical and latitudinal  
512  $\delta^{18}\text{O}_{\text{oce}}$  distribution as in the upper layers of the Atlantic Ocean, while the transition zone  
513 between enrichment and depletion shoals to approx. 1,000m water depth. Below a depth of  
514 approx. 3,500m, depleted AABW ( $\delta^{18}\text{O}_{\text{oce}}$  between -0.4‰ and -0.1‰) fills the entire Pacific.

515 The overall pattern of the Atlantic and Pacific cross sections is in good agreement with a  
516 recent study of the *i*LOVECLIM isotope-enabled EMIC (Roche and Caley, 2013) as well as  
517 with two ocean-only GCM studies (Paul et al., 1999; Xu et al., 2012).

### 518 **4.1.3 Discharge of terrestrial surface water**

519 In Fig. 5a, we show the simulated annual mean values of  $\delta^{18}\text{O}$  for grid cells with a mean  
520 inflow of at least  $200\text{m}^3/\text{s}$ , as simulated by the HD scheme (see Chapter 2.1), to depict the  
521 major river systems on Earth, only. In general, the isotopic composition of a specific river is  
522 closely linked to the  $\delta^{18}\text{O}$  signal of P-E in the catchment area of the particular river. The  
523 strongest depletion of down to  $-12\text{‰}$  is found for river systems of in high northern regions of  
524 Siberia and Alaska, in agreement with observational data (Dodd et al., 2012). For the Rhine,  
525 the simulated isotopic composition in the Netherlands is about  $-7\text{‰}$  to  $-8\text{‰}$ , in good  
526 agreement with available observations, and similar good agreement is found for the  
527 Mackenzie River in the Canadian Arctic with a modelled outflow signal of  $-19\text{‰}$  to  $-20\text{‰}$   
528 (Hoffmann et al., 1998). Rivers in mid- and low latitudes contain in general more enriched  
529 waters, and the PI model experiment results in least depleted waters ( $> -4\text{‰}$ ) for the Paraná  
530 River (Argentina), and the Orange River (South Africa). In the future, the current efforts of  
531 the IAEA to build a systematic database of available isotope measurements in rivers (IAEA,  
532 2012) will allow for a more thoroughly evaluation of these model results.

533 For closing the global water budget, the HD scheme does not only simulate the water  
534 transport via large river systems, but also redistributes all net surplus water of terrestrial P-E  
535 fluxes to a nearby coastal grid point by following orographic gradients. The  $\delta^{18}\text{O}$  values of the  
536 resulting annual mean water inflow of the coastal grid points to the ocean is shown in Fig. 5b.

### 537 **4.1.4 Deuterium excess in meteoric and ocean surface waters**

538 In Fig. 6 we show the simulated dex signal in evaporation, precipitation, and ocean surface  
539 waters. Dex values in the evaporation flux (Fig. 6a) range between  $-2\text{‰}$  and  $+16\text{‰}$ . The  
540 lowest values are found in extreme cold and windy regions of the Arctic, parts of the North  
541 Atlantic and above surface waters of the Antarctic Circumpolar Current (ACC). Further  
542 negative dex values are simulated for parts of the Sahara and the Arabian Peninsula, but these  
543 values occur in regions of extreme low evaporation fluxes from the terrestrial surface and are  
544 not meaningful but represent numerical artefacts, caused by the division of two small  
545 numerical values for calculating the  $\delta^{18}\text{O}$  and  $\delta\text{D}$  values. Maximum dex values of up to  $+14\text{‰}$

546 are detected in various regions of the Earth, both above terrestrial and marine surfaces. The  
547 model results show some agreement to the predicted dex values in evaporation by Pfahl and  
548 Sodemann (2014) but it is very difficult to further evaluate this simulated pattern of dex in  
549 the evaporation flux, as no systematic data collection of this quantity exists, so far. For  
550 precipitation (Fig. 6b), modelled  $\text{dex}_p$  values range between 0‰ and +18‰ with the highest  
551 values in northern parts of the Sahara and a band-like structure covering the mountain regions  
552 of Iraq, the Hindu Kush and large parts of the Himalayan plateau. The lowest values occur in  
553 dry regions of the southern Sahara and the Arabian Peninsula, northern India, and northern  
554 Brazil. The Southern Ocean is another region with simulated low  $\text{dex}_p$  values. For the  
555 Antarctic continent, the large-scale dipole of low (high) dex values in West (East) Antarctica  
556 is well captured by the model. For ocean surface waters (Fig. 6d), the simulated variations in  
557 deuterium excess are an order of magnitude lower than in precipitation and range between -  
558 1.6‰ and +1.6‰. Model results reveal a clear distinction with rather low dex values in mid-  
559 to low-latitudinal Atlantic regions, the highest dex values in the Arctic Ocean and the Baltic  
560 Sea, and rather small variations ( $\pm 0.4\text{‰}$ ) in the remaining oceans. Both positive and negative  
561 anomalies are directly linked to the hydrological balance in the particular regions: In the low-  
562 to mid-latitudinal Atlantic Ocean, a net freshwater export exists. As the evaporated and  
563 exported water masses have a positive dex composition, the remaining ocean surface waters  
564 will become negative in their dex composition due to mass balance. In opposite, a region like  
565 the Baltic Sea has a positive mass balance, i.e. total P-E from the Baltic Sea (including its  
566 catchment area) is positive and the excess water masses flow via the Skagerrak into the  
567 Atlantic Ocean. The surplus of precipitation leads to the positive dex signal in the Baltic Sea.  
568 A similar feature is detected for the Arctic Ocean.

569 To evaluate the simulated global distribution of dex in precipitation and ocean surface waters,  
570 we use again the GNIP and GISS data sets. The plotted station values in Fig. 6c,e do not show  
571 a systematic regional bias of the modelled dex signal in precipitation (Fig. 6c) or ocean  
572 surface waters (Fig. 6e). We note that some of the measured dex values, e.g. a series of GISS  
573 data points in the Southern Indian Ocean, show strong small-scale variations that cannot be  
574 matched due to the coarse horizontal model resolution. However, even on a large-scale  
575 average the model results tend to underestimate the dex values in precipitation with a RMSE  
576 of 2.9‰ while the simulated dex values of ocean surface waters are in general higher (RMSE:  
577 1.8‰) than measurements listed in the GISS database. The modelled slope between the  
578 simulated dex in vapour above the ocean surface and the related relative humidity rh

579 | (-6.3%/(10% rh change)) is very close to the value given by Merlivat and Jouzel (1979),  
580 | though. This-The combination of underestimation (overestimation) of simulated dex values in  
581 | precipitation (ocean surface waters) might indicate that the general description of  
582 | fractionation processes during the evaporation of ocean surface waters, implemented as  
583 | proposed by Merlivat and Jouzel (1979), should be revised and refined. This finding is in  
584 | agreement with recent studies by Steen-Larsen et al. (2014b; 2014a; 2015), which reveal  
585 | substantial deviations of the simulated dex signal in water vapour in Greenland, Bermuda, and  
586 | Iceland, by several atmosphere GCM as compared to laser-based spectroscopy measurements  
587 | of isotopes in water vapour.

## 588 **4.2 Changes of the Last Glacial Maximum**

### 589 **4.2.1 Land surface temperature and precipitation changes**

590 | Due to the prescribed changed glacial ice sheet configuration, changed orbital parameters and  
591 | changed greenhouse gas concentrations the simulated LGM climate on glacier-free terrestrial  
592 | areas is on average -5.9°C colder than the modeled PI climate. Most regions show a rather  
593 | uniform cooling in the range of -4°C to -8°C (Fig. 7a). Exceptionally cold regions are mostly  
594 | adjacent to the prescribed Laurentide and Fennoscandian ice sheet, e.g. part of central North  
595 | America and central Europe. Another region of exceptional cooling is a large part of Siberia  
596 | with a cooling of down to -15°C. The only region with a distinct above-average warming is  
597 | located at Alaska. This region most likely warmed during the LGM due to the increased  
598 | distance to sea ice-covered Arctic ocean regions, caused by the glacial sea-level drop of  
599 | approx. 120m. Our results are in overall agreement with the ensemble-mean LGM changes in  
600 | temperature by the fully coupled climate simulations performed within the PMIP2 and  
601 | CMIP5/PMIP3 projects (not shown; Braconnot et al., 2007; Harrison et al., 2014). These  
602 | simulations also indicate for the LGM a maximum cooling of surface temperature over the ice  
603 | sheets by about -30° and an average cooling of glacier-free land surfaces between -2° and -  
604 | 5°C, except for a colder-than-average Siberian region.

605 | For a comparison with proxy data we compare our model results to the LGM continental  
606 | temperature and precipitation reconstruction by Bartlein et al. (2011). This reconstruction is  
607 | mainly based on subfossil pollen and plant macrofossil data. For the 81 sites contained in the  
608 | temperature dataset of Bartlein et al., the simulated annual mean LGM temperature change is  
609 | in 24 cases (242 cases) more than 2°C warmer (colder) than the reconstructed temperature

610 change (Fig. 7b). While the model-data deviations of LGM warming anomalies range  
611 between +0°C and +20°C, the anomalies of LGM cooling are underestimated by down  
612 to -15°C. Several sites with the largest model-data deviations are located near the border of  
613 the prescribed Laurentide and Fennoscandinavian ice sheets. These deviations might simply  
614 be caused by the rather coarse model resolution of 3.8° x 3.8°, which cannot resolve small-  
615 scale temperature changes close to the prescribed glacier area in sufficient detail.

616 Simulated LGM precipitation changes (Fig. 7c) show a drying of large parts of Siberia and  
617 North America, and smaller parts of South America, Africa and East Asia. A wetting is found  
618 for the region of California, western Europe, the Brazilian Highlands, South Africa and most  
619 parts of Australia. Especially the regions of a wetter LGM climate strongly deviate from older  
620 PMIP2 simulations (Braconnot et al., 2007) but are in good overall agreement with the latest  
621 CMIP5 LGM experiments (Harrison et al., 2014). A comparison of the simulation results with  
622 the precipitation reconstruction by Bartlein et al. (2011) reveals less agreement between  
623 simulated and reconstructed precipitation (Fig. 7c,d). In agreement with the reconstructions,  
624 the model simulates a drying over vast parts of Northern Eurasia and Siberia, as well as dipole  
625 pattern of wetter (drier) conditions south of the margin of the Laurentide ice sheet in western  
626 (eastern) North America. However, the model fails to simulate a drying of Western and  
627 Central Europe during the LGM, as indicated by fossil plant data. Overall, the amplitude of  
628 modelled changes in the hydrological cycle (-4690mm/year to +2750mm/yr) is weaker than  
629 the range of the reconstructed changes (-1240mm/yr to +720mm/yr), and the general  
630 underestimation of LGM dryness is in line with model results from the PMIP2 and  
631 CMIP5/PMIP3 projects (Harrison et al., 2014).

#### 632 **4.2.2 LGM changes of $\delta^{18}\text{O}$ in precipitation**

633 Previous studies have already shown that the colder climate of the LGM leads to generally  
634 more depleted  $\delta^{18}\text{O}_p$  values in precipitation (Lee et al., 2008; Risi et al., 2010a). This  
635 depletion is a direct consequence of the changed (temperature-dependent) fractionation  
636 strength during both evaporation and condensation processes. Over glacier-free land surfaces,  
637 we calculate a precipitation-weighted mean decrease of  $\delta^{18}\text{O}_p$  in precipitation by -0.24‰. For  
638 tropical and sub-tropical regions in Mid- and South America, Africa, Australia, and parts of  
639 Asia, our simulation reveals almost no LGM-PI changes in  $\delta^{18}\text{O}_p$  in precipitation (Fig. 8a).  
640 Glacial changes of down to -3‰ occur in precipitation over the southern parts of South  
641 America and Africa, the Tibetan Plateau, as well as over major parts of Siberia, North



642 America, and Alaska. The strongest simulated LGM-PI changes of  $\delta^{18}\text{O}_p$  in precipitation  
643 (down to -12‰) are found over the glacier areas of both the Northern and Southern  
644 Hemisphere. We restrict a first quantitative evaluation of the simulated LGM-PI  $\delta^{18}\text{O}_p$   
645 anomalies in precipitation to the chosen data of 21 ice cores (Table 1) and 8 speleothem  
646 records (Table 2). Our dataset is partly identical to the one used by Risi et al. (2010a) and by  
647 Brennan et al. (2012) and enables a direct comparison with these previous model studies. For  
648 the ice core records, we compare the modelled change of  $\delta^{18}\text{O}_p$  in precipitation with the ice  
649 core data (Table 1). For the speleothem records, we use both the simulated LGM-PI  
650 temperature and  $\delta^{18}\text{O}_p$  changes to calculate the modelled change of  $\delta^{18}\text{O}_c$  in calcite, which is  
651 then compared ~~the model results~~ with the reconstructions (Table 2). Overall, the model results  
652 agree well ( $r^2 = 0.64$ , RMSE = 2.78‰) with the reconstructed LGM-PI  $\delta^{18}\text{O}_p$  changes at the  
653 various sites (Fig. 8b). The largest deviations are found for the Camp Century ice core  
654 (measured LGM-PI  $\delta^{18}\text{O}_p$  difference: -12.9‰, modelled: -9.54‰) and for the  $\delta^{18}\text{O}_p$  in  
655 precipitation at 4 out of 5 tropical ice core locations.

656 From the simulated LGM-PI temperature and  $\delta^{18}\text{O}_p$  changes we calculate the temporal  $\delta^{18}\text{O}_p$ -  
657 T-gradient  $m$  in a specific grid box as  $m = (\delta^{18}\text{O}_{p, \text{LGM}} - \delta^{18}\text{O}_{p, \text{PI}}) / (T_{\text{LGM}} - T_{\text{PI}})$ , with  $T$  as the  
658 surface temperature at the precipitation site. We restrict our calculation to mid- and high-  
659 latitude regions with an annual mean PI temperature  $T_{\text{PI}}$  below +20°C. As a further selection  
660 criteria, we use grid cells with a simulated LGM-PI cooling of at least -2°C, only. The  
661 calculated temporal  $\delta^{18}\text{O}_p$ -T-gradient  $m$  for the selected grid cells ( $N = 1195$ ) ranges between  
662 -0.53 and +0.85 (Fig. 8c). For only 187% of the grid cells ( $N = 198218$ ), the calculated  
663 temporal  $\delta^{18}\text{O}_p$ -T-gradient ranges between +0.5‰/°C and +0.7‰/°C, close to the simulated  
664 modern spatial  $\delta^{18}\text{O}_p$ -T-gradient of  $m = 0.58\text{‰}/\text{°C}$  (see Chapter 4.1.1). In a vast majority of  
665 the grid cells (8979%), the temporal  $\delta^{18}\text{O}_p$ -T-gradient is below the modern spatial one, while  
666 a higher temporal gradient is simulated for 3% of the selected cells, only. A clear difference  
667 between temporal and spatial  $\delta^{18}\text{O}_p$ -T-gradient has already been reported for Greenland  
668 (Buizert et al., 2014; Jouzel, 1999; Werner et al., 2000) and might be caused by different  
669 mechanisms (e.g., change in precipitation seasonality, shift of water vapour source regions  
670 and transport pathways, varying vertical temperature gradients and atmospheric heights of  
671 precipitation formation). However, our results indicate that such a potential bias of the  $\delta^{18}\text{O}_p$ -  
672 thermometer (if a modern spatial  $\delta^{18}\text{O}_p$ -T-gradient is used for past temperature  
673 reconstructions) might not exist for Greenland, only, but also for large parts of the mid- and

674 high-latitude regions. The robustness and implications of these findings will be further  
675 investigated in future studies.

676 Next, we take a more detailed look at the simulation results over both polar ice caps. For the  
677 extended compilation of ice core data listed in Table 1, our model results are in good  
678 agreement with glacial  $\delta^{18}\text{O}_p$  anomalies found in Antarctic ice cores (Fig. 9). Mean model-  
679 data deviation is 1.1‰ with the largest mismatch for the Byrd ice core (2.35‰). For  
680 Greenland, model-data differences are slightly higher than for Antarctica as the model  
681 underestimates the LGM-PI  $\delta^{18}\text{O}_p$  changes by 1.56‰, on average. As already noted above,  
682 the largest mismatch is found for the Camp Century ice core (3.45‰). The reason for this  
683 stronger model-data mismatch for Greenland as compared to Antarctica could be partly due to  
684 the coarse model resolution, or caused by an erroneous warm bias of SST in the source  
685 regions of vapour transported to Greenland. Testing and evaluating these different hypotheses  
686 will require further coupled simulations and analyses.

#### 687 **4.2.3 LGM changes of ocean temperatures and marine $\delta^{18}\text{O}$ signals**

688 The state of the glacial oceans has been under debate since the first reconstruction of global  
689 LGM sea surface temperatures (SST) and sea ice coverage by the CLIMAP group (CLIMAP  
690 Project Members, 1976). As compared to CLIMAP, the most recent SST reconstruction by  
691 the MARGO project (MARGO Project Members, 2009) indicates, among others, a more  
692 pronounced cooling in the eastern mid-latitude North Atlantic than in the western basin, ice-  
693 free conditions in the Nordic seas during glacial summer, as well as a 1°C - 3°C cooling of the  
694 western Pacific warm pool. The study also revealed the presence of large longitudinal  
695 gradients in LGM SST anomalies in all the ocean basins, which are absent in the majority of  
696 atmosphere-ocean coupled simulations of the PMIP2 project (MARGO Project Members,  
697 2009).

698 The physical state of the glacial ocean of our LGM simulation has already been analysed and  
699 described in detail by Zhang et al (2013). In agreement with this previous study, we also find  
700 a rather uniform SST cooling in the range of 2°C – 4°C during the LGM in our simulation,  
701 comparable to the results of several atmosphere-ocean GCM participating in PMIP2 and  
702 CMIP5/PMIP3 (Zhuang and Giardino, 2012). For the isotopic composition of ocean surface  
703 waters  $\delta^{18}\text{O}_{\text{oce}}$ , we simulate a globally averaged mean increase of +0.84‰ as compared to the  
704 PI ocean state. This is noteworthy, as we adjusted in our LGM simulation the global ocean  
705 isotopic composition by +1‰ to account for the change in global ice volume. A less-than-

706 average part of this increase (0.94‰) is found in surface and shallow water depth down to  
707 approx. 1000m, while deeper water masses show a glacial increase of up to +1.06‰ in our  
708 simulation. In addition, the simulated glacial increase is not spatially uniform for the ocean  
709 surface waters, neither. For most regions the LGM anomalies are in the order of +0.5‰ to  
710 +1‰ (Fig. 10a), but more positive LGM  $\delta^{18}\text{O}_{\text{oce}}$  anomalies exist in the ACC region (up to  
711 +1.5‰), the Mediterranean region (up to +3‰), as well as in the North Atlantic region above  
712 approx. 30°N (up to +2.3‰).

713 As both water temperatures and  $\delta^{18}\text{O}_{\text{oce}}$  are explicitly simulated by our model setup, we can  
714 calculate  $\delta^{18}\text{O}_{\text{c(PDB)}}$  for the PI and LGM simulation and then compare our model results to the  
715 marine calcite  $\delta^{18}\text{O}_{\text{c}}$  dataset documented by Caley et al. (2014b). In agreement with the  
716 simulated pattern of LGM  $\delta^{18}\text{O}_{\text{oce}}$  anomalies in seawater, the simulated  $\delta^{18}\text{O}_{\text{c}}$  changes in  
717 calcite are strongest in the ACC region, the Mediterranean Sea and the North Atlantic.  
718 Positive  $\delta^{18}\text{O}_{\text{c}}$  anomalies reach maximum values of +2.6‰ in the North Atlantic. Comparing  
719 the pattern of simulated LGM-PI changes of  $\delta^{18}\text{O}_{\text{oce}}$  in surface waters (Fig. 10a) and  $\delta^{18}\text{O}_{\text{c}}$  in  
720 calcite (Fig. 10b) it is also noteworthy that (a) there exists an additional strong positive LGM  
721  $\delta^{18}\text{O}_{\text{c}}$  anomaly in the East China Sea and parts of the North Pacific, which has no counterpart  
722 in the  $\delta^{18}\text{O}_{\text{oce}}$  changes of ocean surface waters, (b) the  $\delta^{18}\text{O}_{\text{c}}$  anomalies in the Pacific ACC  
723 region are shifted northwards by approx. 5° as compared to the  $\delta^{18}\text{O}_{\text{oce}}$  surface waters  
724 anomalies.

725 A comparison of the simulated  $\delta^{18}\text{O}_{\text{c}}$  values in ocean surface waters between 0-50m to the  
726  $\delta^{18}\text{O}_{\text{c}}$  data set of planktic LGM  $\delta^{18}\text{O}_{\text{c}}$  anomalies compiled by Caley et al. (2014b) shows a  
727 systematic overestimation of simulated LGM  $\delta^{18}\text{O}_{\text{c}}$  changes for the Mediterranean Sea (Fig.  
728 10c). For all three major oceans, our model simulation both underestimates and overestimates  
729 LGM  $\delta^{18}\text{O}_{\text{c}}$  changes at various marine sediment sites. Model-data differences are mostly  
730 within the order of the reported uncertainty of the reconstructed LGM  $\delta^{18}\text{O}_{\text{c}}$  anomalies, as  
731 reported by Caley et al. (2014b). The simulated spatial pattern of LGM  $\delta^{18}\text{O}_{\text{c}}$  anomalies in  
732 surface waters shows some remarkable resemblance to the model results of Caley et al.  
733 (2014b) using the iLOVECLIM model. In their study, Caley et al. also find the strongest  
734 positive  $\delta^{18}\text{O}_{\text{c}}$  anomalies in the North Atlantic, parts of the northern Pacific as well as in the  
735 ACC. In contrast to our simulation, Caley et al. report an additional strong  $\delta^{18}\text{O}_{\text{c}}$  anomaly in  
736 the northern Indian Ocean.

737 In Fig. 11 mean LGM-PI changes of  $\delta^{18}\text{O}_c$  for the Atlantic cross section ( $60^\circ\text{W}$ - $0^\circ\text{W}$ ) and the  
738 Pacific cross section ( $150^\circ\text{E}$  to  $110^\circ\text{W}$ ) are shown. For both oceans, model results show the  
739 strongest positive change of  $\delta^{18}\text{O}_c$  between 500m and 3,000m. While  $\delta^{18}\text{O}_c$  changes of up to  
740  $+2.6\text{‰}$  are simulated at around  $30^\circ\text{N}$  for the Atlantic basin, the  $\delta^{18}\text{O}_c$  changes in the Pacific  
741 water masses are in general lower (up to  $+2.2\text{‰}$ ) and the region of the largest change is  
742 located between  $0^\circ$  and  $50^\circ\text{S}$ . The available benthic foraminifera data compiled by Caley et al.  
743 (2014b) partly supports these findings. The too positive modelled  $\delta^{18}\text{O}_c$  values in the North  
744 Atlantic in a depth between approx. 2,500m and 4,000m indicate that the simulated NADW  
745 formation is probably too strong and too deep. By combining a series of isotope studies with  
746 different NADW strengths with available proxy studies of the glacial NADW formation  
747 (Duplessy et al., 1980) it should be possible to constrain and improve this aspect of the  
748 isotope-enhanced version of the ECHAM5/MPI-OM model. Recently, Roche et al. (2014)  
749 presented a similar approach for an improved modelling of Heinrich event 1. However,  
750 performing such a set of fully coupled sensitivity experiments is computationally demanding  
751 and beyond the scope of this paper.

#### 752 **4.2.4 Glacial changes of the deuterium excess**

753 In Fig. 12a, we show the global pattern of simulated LGM-PI dex anomalies in precipitation  
754 over land surfaces. Changes are rather minor, in the order of  $-3\text{‰}$  to  $+3\text{‰}$ , except for a clear  
755 positive anomaly (up to  $+6\text{‰}$ ) in North America south-west of the Laurentide ice sheet  
756 margin, and strong negative anomalies (down to  $-7\text{‰}$ ) above Greenland and Antarctica. For  
757 ocean surface waters, the simulated dex anomalies are even smaller and almost everywhere in  
758 the range of  $\pm 1\text{‰}$  (not shown). Figure 12b shows the simulated LGM-PI dex anomalies in  
759 water vapour of the lowest atmospheric model layer above the ocean surface (discussed  
760 below).

761 As stated in Chapter 2, we assumed no glacial change of the mean deuterium excess signal in  
762 the glacial ocean. However, some recent data (Schrag et al., 2002) suggest a mean glacial dD  
763 increase of  $+7.2\text{‰}$ , which is slightly lower than the increase prescribed in our LGM  
764 simulation ( $+8\text{‰}$ ). Such lower glacial dD increase would lead to a mean glacial change of the  
765 deuterium excess in ocean waters of  $-0.8\text{‰}$ . As a first-order estimate, such lowered deuterium  
766 excess signal in the ocean might lead to an equivalent lower deuterium excess value both in  
767 vapour above the ocean and, consequently, in precipitation, too.

768 So far, ice cores are the only paleoproxy archive, which allow for reconstructing past changes  
769 of deuterium excess values in precipitation. In Fig. 13 we compare our model results of  
770 annual mean dex changes in precipitation between the LGM and PI simulation with the  
771 compiled ice core data (Table 21). Mean absolute deviation between modelled LGM-PI  
772 anomalies and ice core data from Antarctica is 1.6‰. For Greenland ice cores, LGM dex  
773 values have been only reported for the GRIP ice core, so far. Here, model results  
774 underestimate the LGM-PI dex change by 2‰. The overall good agreement between  
775 measured and modelled LGM dex changes is remarkable, as isotope-enabled GCM have had  
776 some difficulties simulating the measured LGM dex changes in Antarctic ice cores, so far  
777 (e.g., Risi et al., 2010a; Werner et al., 2001). As dex values in polar ice cores depend on  
778 climate condition during evaporation of the source water, and as the SST of our simulation are  
779 more uniform and lower than the latest MARGO reconstruction, one may ask if the good dex  
780 agreement is due to the modelled SST. For testing this hypothesis we have conducted an  
781 atmosphere-only ECHAM5-wiso simulation with identical LGM boundary conditions as for  
782 the fully-coupled ECHAM5/MPI-OM setup but using the GLAMAP LGM SST  
783 reconstruction, which was supplemented by older CLIMAP data in order to have global  
784 coverage (Schäfer-Neth and Paul, 2003a; 2003b). For  $\delta^{18}\text{O}_{\text{oce}}$  ( $\delta\text{D}_{\text{oce}}$ ), we prescribed a uniform  
785 glacial increase of +1‰ (+8‰) in this simulation. In this ECHAM5-wiso sensitivity study,  
786 the relatively warm (sub)tropical GLAMAP SST reconstruction leads to smaller simulated  
787 negative dex anomalies, or even slightly positive dex anomalies for Vostok and Dome F (Fig.  
788 13). The RMSE of all Antarctic ice cores is 2.3‰, which is 0.7‰ worse than in the fully-  
789 coupled simulation. We are aware that such a comparison of the fully coupled  
790 ECHAM5/MPI-OM setup with an atmosphere-only ECHAM5 experiment with prescribed  
791 SST might be hampered by neglecting any atmosphere-ocean feedback in the later.  
792 Nevertheless, our simulations indicate that glacial SST, which are cooler than the GLAMAP  
793 reconstruction, lead to an improved simulation of dex changes, at least over Antarctica.  
794 However, for Greenland the simulated dex anomaly at the GRIP drilling site becomes too low  
795 in our fully coupled simulation. But as no more LGM-PI dex records of Greenland ice core  
796 records have been published, yet, it remains an open question if this deviation points to a  
797 systematic bias in our simulation. More LGM-PI dex data from polar ice cores in combination  
798 with further isotope simulations are required to put an additional, highly valuable constraint  
799 on available LGM SST reconstructions.

800 Apart from glacial SST changes, changes in the source areas of water transported to  
801 Antarctica and Greenland, e.g. by a glacial change in sea ice coverage, might lead to the  
802 change in the deuterium excess signal in polar precipitation, too. The simulated sea ice  
803 coverage of the COSMOS LGM simulation has already been described in detail in Zhang et  
804 al. (2013) and our simulation results are comparable to this previous study. For the southern  
805 hemisphere, there is a reasonable agreement between the simulated sea ice concentration and  
806 proxy data by Gersonde et al. (2005), such as the austral winter sea ice extent in the Atlantic  
807 sector and the austral summer sea ice extent in the Indian ocean sector. However, the  
808 simulation might underestimate a larger extent of sporadic summer sea ice between 5°E and  
809 5°W in the Southern Ocean, as discussed in Gersonde et al. (2005). As compared to the  
810 ECHAM5 experiment with GLAMAP data, a much-reduced sea ice cover in austral summer  
811 is found in this coupled ECHAM5/MPI-ESM LGM simulation. This reduction might lead to a  
812 stronger contribution of vapour stemming from regions between 60°-65°S to the Antarctic ice  
813 sheet. As vapour from these regions has a strong negative deuterium excess signal (cf. Fig.  
814 12) such shift in the source contributions might lead to a more negative deuterium excess  
815 signal in Antarctic precipitation, too.

816 Pfahl and Soedemann (2014) suggest in their study that the typical interpretation of dex  
817 variations in ice core records as SST changes might have to be adapted to reflect climatic  
818 influences on relative humidity during evaporation. To test this hypothesis, we look at the  
819 simulated LGM-PI dex anomalies in water vapour of the lowest atmospheric layer, directly  
820 above the ocean surface (Fig. 12b). It is safe to assume that most water transported to  
821 Antarctica will stem from Southern Hemisphere marine vapour source regions, and not from  
822 continental vapour sources. Simulated LGM-PI dex anomalies of the vapour vary between  
823 0‰ and -5‰ for most ocean regions with a clear gradient towards more negative dex values  
824 in the higher latitudinal regions. Plotting these simulated changes of dex in vapour against the  
825 modelled relative humidity change between LGM and PI over the ocean surface reveals no  
826 correlation between these humidity changes and the simulated dex variations in the vapour  
827 layer. As seen in Fig. 14a, simulated LGM values of the relative humidity of the vapour layer  
828 above ocean surface varies just by  $\pm 5\%$  as compared to the PI values. These rather small  
829 variations of the LGM relative humidity changes are somewhat surprising, as cooler SST  
830 should lead to cooler air temperatures above the ocean surface, which then should lead to  
831 higher relative humidity levels (if the amount of water in the air stays constant). However, we  
832 find in our simulations that the air directly above the ocean surface cools slightly stronger

833 during the LGM than the SST themselves. This leads to a reduced glacial evaporation flux  
834 from the ocean to the atmosphere, which decreases the relative humidity of the vapour and  
835 counterbalance the first effect. Similar small changes of relative humidity changes above the  
836 ocean surface and the counterbalance of different effects have recently been reported for a set  
837 of CMIP5 climate model results by Laîné et al. (2014). They have analysed a future warmer  
838 climate, though. In contrast, modelled LGM SST changes of the Southern Hemisphere cover a  
839 range of 0°C to -15°C, and a strong correlation ( $r^2 = 0.78$ ) between simulated glacial SST  
840 changes and LGM dex anomalies in the vapour above the ocean surface is found (Fig. 14b).  
841 We rate this finding as a support of the ‘classical’ interpretation of dex changes in Antarctic  
842 ice cores as a proxy for SST changes in the source regions of water transported to Antarctica.  
843 However, the correlation between vapour dex and SST changes does not rule out other  
844 influencing factors, like wind speed changes, which might affect both the deuterium excess  
845 signal and SST changes, simultaneously. Furthermore, –we are aware that several recent  
846 studies of dex in water vapour have revealed a large bias between measurements and  
847 simulations by different isotope-enabled atmospheric GCM (Steen-Larsen et al., 2014b;  
848 2015). We cannot resolve this conundrum with the performed simulations and will investigate  
849 this topic in more detail in the future.

## 850 **5 Summary and Conclusions**

851 In this study we present the first simulations of the fully coupled Earth System Model  
852 ECHAM5/MPI-OM. The model has been enhanced by an explicit stable water isotope  
853 diagnostics in all relevant model components: atmosphere, land surface, terrestrial discharge,  
854 and ocean. The hydrological cycle and its isotopic balance are fully closed in the model setup,  
855 and the model has been run successfully into equilibrium under PI and LGM boundary  
856 conditions.

857 First-order isotope variations in precipitation ( $\delta^{18}\text{O}_p$ ,  $\delta\text{D}_p$ ) for the PI and LGM climate are in  
858 good to very good agreement with available present-day observations from the GNIP  
859 database, and with LGM isotope data from various ice core and speleothem records. The  
860 largest  $\delta$ -deviations between present-day observations and model results are found in high-  
861 latitudinal regions and are caused by a warm bias of the coupled model, similar to the  
862 reported error of the atmosphere-only GCM ECHAM5-wiso (Werner et al., 2011). Such a

863 warm bias, especially over Antarctica, is frequent in GCM (Masson-Delmotte et al., 2006)  
864 and is partly related to the coarse spatial resolution of our model setup.

865 The simulated modern spatial  $\delta$ -T-relation is also in good agreement with the observed one,  
866 based on a selection of GNIP and ice core data. A first assessment of the stability of this  
867 relation for LGM-PI climate changes reveals that the temporal  $\delta$ -T-gradient might have been  
868 substantially lower than the modern spatial one for most mid- to high-latitude regions. Such  
869 a deviation, which causes a strong bias in the 'classical'  $\delta$ -paleothermometry approach, is  
870 known for Greenland ice cores (Jouzel, 1999) but has not been discussed for other Northern  
871 Hemisphere regions, so far. Future in-depth analyses of our model results can help to achieve  
872 an improved interpretation of available isotope records, e.g. from speleothems or permafrost  
873 ice wedges (Meyer et al., 2015), from these regions.

874 For the PI climate, simulated marine  $\delta^{18}\text{O}_{\text{oce}}$  values broadly fit to available measurements  
875 compiled in the GISS database. For the Atlantic, Pacific, and Indian Ocean the largest model-  
876 data deviations in ocean surface waters are found in the vicinity of large river estuaries, the  
877 Sea of Okhotsk, parts of the Bering Sea, and the Baltic Sea. Like for the model deficits in  
878  $\delta^{18}\text{O}_{\text{p}}$ , these deviations are most likely related to the rather coarse resolution of the ocean  
879 model component MPI-OM, which hampers a realistic simulation of water mass mixing in  
880 these coastal regions. For the Arctic, modelled  $\delta^{18}\text{O}_{\text{oce}}$  values in surface waters show a more  
881 general negative bias as compared to the GISS data. It remains an open question if this bias  
882 can also be simply related to an inadequate mixing of the isotopically depleted inflow of  
883 Arctic rivers into this ocean basin, or if a more general model bias in the hydrological balance  
884 of the Arctic Ocean exists. For the simulated LGM  $\delta^{18}\text{O}$  changes, a comparison of model  
885 results with available  $\delta^{18}\text{O}_{\text{c}}$  calcite data from planktic and benthic foraminifera shells reveals a  
886 partly model-data match, only. For the North Atlantic, the modelled glacial NADW formation  
887 appears too deep and too strong in our LGM simulation. However, more sensitivity studies  
888 are necessary to better constrain this aspect of glacial ocean circulation change. As a next  
889 step, we will also more explicitly simulate the dependence of  $\delta^{18}\text{O}_{\text{c}}$  on the surrounding water  
890 conditions, and analyse the stability of the relation between  $\delta^{18}\text{O}$  and salinity in ocean waters  
891 under the different climate conditions.

892 The simulation results for second-order changes of  $\delta^{18}\text{O}$  and  $\delta\text{D}$  are also satisfactory. In our  
893 analyses, an overall good fit of modern deuterium excess values in precipitation and ocean  
894 surface waters with the available observations is found. However, on large-scale average the



895 ECHAM5/MPI-OM isotope results tend to slightly underestimate the dex values in  
896 precipitation and, at the same time, overestimate the simulated dex values of ocean surface  
897 waters. This combination of opposite biases suggests that the implementation of fractionation  
898 processes during the evaporation of ocean surface waters in our model setup, which is strictly  
899 following the approach by Merlivat and Jouzel (1979), should maybe be revised and refined  
900 in future studies. For LGM-PI changes of deuterium excess, only measurements from  
901 Greenland and Antarctic ice cores are available, at present. Our simulation results indicate  
902 that LGM Southern Hemisphere SST, which are cooler than the ~~CLIMAP~~-MARGO  
903 reconstruction, lead to an improved simulation of dex values in Antarctic precipitation. In  
904 addition, our analyses reveal that modelled glacial dex changes are strongly correlation to  
905 LGM-PI SST changes, but not to relative humidity changes in the evaporation regions.

906 In this study we have presented first results of the newly developed isotope-enabled version of  
907 the Earth System Model ECHAM5/MPI-OM. We have focused on two equilibrium  
908 simulations under the pre-industrial and last glacial maximum period, only, due to their  
909 different climate states and the wealth of available observational data from both periods.  
910 Future studies will investigate changes in the hydrological cycle and its isotopic composition  
911 for further climate periods of the past, e.g. the last interglacial, as well as for the transition  
912 between them.

913

914

915 **References**

- 916 Baertschi, P.: Absolute  $^{18}\text{O}$  content of standard mean ocean water, *Earth Planet. Sci. Lett.*,  
917 31(3), 341–344, doi: 10.1016/0012-821X(76)90115-1, 1976.
- 918 Bartlein, P. J., Harrison, S. P., Brewer, S., Connor, S., Davis, B. A. S., Gajewski, K., Guiot, J.,  
919 Harrison-Prentice, T. I., Henderson, A., Peyron, O., Prentice, I. C., Scholze, M., Seppä, H.,  
920 Shuman, B., Sugita, S., Thompson, R. S., Viau, A. E., Williams, J. and Wu, H.: Pollen-  
921 based continental climate reconstructions at 6 and 21ka: a global synthesis, *Clim. Dyn.*,  
922 37(3-4), 775–802, doi: 10.1007/s00382-010-0904-1, 2011.
- 923 Bigg, G. R. and Rohling, E. J.: An oxygen isotope data set for marine waters, *J. Geophys.*  
924 *Res. Oceans*, 105(C4), 8527–8535, 2000.
- 925 Bonne, J. L., Masson-Delmotte, V., Cattani, O., Delmotte, M., Risi, C., Sodemann, H. and  
926 Steen-Larsen, H. C.: The isotopic composition of water vapour and precipitation in  
927 Ivittuut, southern Greenland, *Atmos. Chem. Phys.*, 14(9), 4419–4439, doi: 10.5194/acp-14-  
928 4419-2014-supplement, 2014.
- 929 Braconnot, P., Otto-Bliesner, B., Harrison, S., Joussaume, S., Peterchmitt, J. Y., Abe-Ouchi,  
930 A., Crucifix, M., Driesschaert, E., Fichet, T., Hewitt, C. D., Kageyama, M., Kitoh, A.,  
931 Laine, A., Loutre, M. F., Marti, O., Merkel, U., Ramstein, G., Valdes, P., Weber, S. L., Yu,  
932 Y. and Zhao, Y.: Results of PMIP2 coupled simulations of the Mid-Holocene and Last  
933 Glacial Maximum - Part 1: experiments and large-scale features, *Clim Past*, 3(2), 261–277,  
934 2007.
- 935 Brennan, C. E., Weaver, A. J., Eby, M. and Meissner, K. J.: Modelling oxygen isotopes in the  
936 University of Victoria Earth System Climate Model for pre-industrial and last glacial  
937 maximum conditions, *Atmosphere-Ocean*, 50(4), 447–465, doi:  
938 10.1080/07055900.2012.707611, 2012.
- 939 Broecker, W. S., Peng, T. H., Jouzel, J. and Russell, G.: The magnitude of global fresh-water  
940 transports of importance to ocean circulation, *Clim. Dyn.*, 4(2), 73–79, doi:  
941 10.1007/BF00208902, 1990.
- 942 Brovkin, V., Raddatz, T., Reick, C. H., Claussen, M. and Gayler, V.: Global biogeophysical  
943 interactions between forest and climate, *Geophys. Res. Lett.*, 36, doi:  
944 10.1029/2009gl037543, 2009.
- 945 Buizert, C., Gkinis, V., Severinghaus, J. P., He, F., Lecavalier, B. S., Kindler, P.,  
946 Leuenberger, M., Carlson, A. E., Vinther, B., Masson-Delmotte, V., White, J. W. C., Liu,  
947 Z., Otto-Bliesner, B. and Brook, E. J.: Greenland temperature response to climate forcing  
948 during the last deglaciation, *Science*, 345(6201), 1177–1180, 2014.
- 949 [Caley, T., Roche, D. M. and Renssen, H.: Orbital Asian summer monsoon dynamics revealed](#)  
950 [using an isotope-enabled global climate model, \*Nature Communications\*, 5,](#)  
951 [doi:10.1038/ncomms6371, 2014a.](#)
- 952 Caley, T., Roche, D. M., Waelbroeck, C. and Michel, E.: Oxygen stable isotopes during the  
953 Last Glacial Maximum climate: perspectives from data–model (iLOVECLIM) comparison,  
954 *Clim Past*, 10(6), 1939–1955, doi: 10.5194/cp-10-1939-2014, 2014b.
- 955 CLIMAP Project Members: Surface of Ice-Age Earth, *Science*, 191(4232), 1131–1137, 1976.
- 956 ~~Coplen, T. B.: Normalization of oxygen and hydrogen isotope data, *Chem Geol*, 72(4), 293–~~  
957 ~~297, doi: 10.1016/0168-9622(88)90042-5, 1988.~~
- 958 ~~Coplen, T. B., Kendall, C., and Hopple, J.: Comparison of stable isotope reference samples,~~  
959 ~~*Nature*, 302, 236–238, 1983.~~

- 960 Craig, H. and Gordon, L. I.: Deuterium and oxygen 18 variations in the ocean and the marine  
 961 atmosphere, edited by E. Tongiogi, pp. 9–130, Consiglio nazionale delle ricerche,  
 962 Laboratorio de geologia nucleare, Spoleto, Italy. 1965.
- 963 Cruz, F. W., Burns, S. J., Karmann, I., Sharp, W. D., Vuille, M., Cardoso, A. O., Ferrari, J.  
 964 A., Dias, P. L. S. and Viana, O.: Insolation-driven changes in atmospheric circulation over  
 965 the past 116,000 years in subtropical Brazil, *Nature*, 434(7029), 63–66, doi:  
 966 10.1038/Nature03365, 2005.
- 967 Dansgaard, W.: Stable isotopes in precipitation, *Tellus*, 16(4), 436–468, 1964.
- 968 Dansgaard, W., Johnsen, S. J., Møller, J. and Langway, C. C.: Oxygen isotope record for the  
 969 Camp Century Greenland ice core, *Science*, 166, 377, 1969.
- 970 [Dayem, K. E., Molnar, P., Battisti, D. S. and Roe, G. H.: Lessons learned from oxygen](#)  
 971 [isotopes in modern precipitation applied to interpretation of speleothem records of](#)  
 972 [paleoclimate from eastern Asia, \*Earth Planet. Sci. Lett.\*, 295\(1-2\), 219–230,](#)  
 973 [doi:10.1016/j.epsl.2010.04.003, 2010.](#)
- 974 de Wit, J. C., van der Straaten, C. M. and Mook, W. G.: Determination of the absolute  
 975 hydrogen isotopic ratio of V-SMOW and SLAP, *Geostandards Newsletter*, 4(1), 33–36,  
 976 doi: 10.1111/j.1751-908X.1980.tb00270.x, 1980.
- 977 Dee, D. P., Uppala, S. M., Simmons, A. J., Berrisford, P., Poli, P., Kobayashi, S., Andrae, U.,  
 978 Balmaseda, M. A., Balsamo, G., Bauer, P., Bechtold, P., Beljaars, A. C. M., van de Berg,  
 979 L., Bidlot, J., Bormann, N., Delsol, C., Dragani, R., Fuentes, M., Geer, A. J., Haimberger,  
 980 L., Healy, S. B., Hersbach, H., Holm, E. V., Isaksen, L., Kallberg, P., Kohler, M.,  
 981 Matricardi, M., McNally, A. P., Monge-Sanz, B. M., Morcrette, J. J., Park, B. K., Peubey,  
 982 C., de Rosnay, P., Tavolato, C., Thepaut, J. N. and Vitart, F.: The ERA-Interim reanalysis:  
 983 configuration and performance of the data assimilation system, *Q. J. Roy. Meteor. Soc.*,  
 984 137(656), 553–597, doi: 10.1002/Qj.828, 2011.
- 985 Delaygue, G., Jouzel, J. and Dutay, J. C.: Oxygen 18-salinity relationship simulated by an  
 986 oceanic general circulation model, *Earth Planet. Sci. Lett.*, 178(1-2), 113–123, doi:  
 987 10.1016/S0012-821X(00)00073-X, 2000.
- 988 Dodd, P. A., Rabe, B., Hansen, E., Falck, E., Mackensen, A., Rohling, E., Stedmon, C. and  
 989 Kristiansen, S.: The freshwater composition of the Fram Strait outflow derived from a  
 990 decade of tracer measurements, *J. Geophys. Res.*, 117(C11), C11005, 2012.
- 991 Dreybrodt, W. and Scholz, D.: Climatic dependence of stable carbon and oxygen isotope  
 992 signals recorded in speleothems: From soil water to speleothem calcite, *Geochim.*  
 993 *Cosmochim. Acta*, 75(3), 734–752, doi: 10.1016/j.gca.2010.11.002, 2011.
- 994 Duplessy, J. C., Moyes, J. and Pujol, C.: Deep-water formation in the North-Atlantic Ocean  
 995 during the last Ice-Age, *Nature*, 286(5772), 479–482, 1980.
- 996 Fleitmann, D., Burns, S. J., Mudelsee, M., Neff, U., Kramers, J., Mangini, A. and Matter, A.:  
 997 Holocene Forcing of the Indian Monsoon Recorded in a Stalagmite from Southern Oman,  
 998 *Science*, 300(5626), 1737–1739, doi: 10.1126/science.1083130, 2003.
- 999 [Gersonde, R., Crosta, X., Abelmann, A. and Armand, L.: Sea-surface temperature and sea ice](#)  
 1000 [distribution of the Southern Ocean at the EPILOG Last Glacial Maximum - A circum-](#)  
 1001 [Antarctic view based on siliceous microfossil records, \*Quaternary Sci Rev\*, 24\(7-9\), 869–](#)  
 1002 [896, doi:10.1016/j.quascirev.2004.07.015, 2005.](#)
- 1003 Haese, B., Werner, M. and Lohmann, G.: Stable water isotopes in the coupled atmosphere–  
 1004 land surface model ECHAM5-JSBACH, *Geosci. Model Dev.*, 6(5), 1463–1480, doi:  
 1005 10.5194/gmd-6-1463-2013, 2013.

- 1006 Hagemann, S. and Gates, L. D.: Improving a subgrid runoff parameterization scheme for  
 1007 climate models by the use of high resolution data derived from satellite observations, *Clim.*  
 1008 *Dyn.*, 21(3-4), 349–359, doi: 10.1007/s00382-003-0349-x, 2003.
- 1009 Harrison, S. P., Bartlein, P. J., Brewer, S., Prentice, I. C., Boyd, M., Hessler, I., Holmgren, K.,  
 1010 Izumi, K. and Willis, K.: Climate model benchmarking with glacial and mid-Holocene  
 1011 climates, *Clim. Dyn.*, 43(3-4), 671–688, doi: 10.1007/s00382-013-1922-6, 2014.
- 1012 Hibler, W. D.: A dynamic thermodynamic sea ice model, *J. Phys. Oceanogr.*, 9(4), 815–846,  
 1013 1979.
- 1014 Hoffmann, G., Werner, M. and Heimann, M.: Water isotope module of the ECHAM  
 1015 atmospheric general circulation model: A study on timescales from days to several years, *J.*  
 1016 *Geophys. Res. Atmos.*, 103(D14), 16871–16896, 1998.
- 1017 Hoffmann, G., Ramirez, E., Taupin, J. D., Francou, B., Ribstein, P., Delmas, R., Durr, H.,  
 1018 Gallaire, R., Simoes, J., Schotterer, U., Stiévenard, M. and Werner, M.: Coherent isotope  
 1019 history of Andean ice cores over the last century, *Geophys. Res. Lett.*, 30(4), doi:  
 1020 10.1029/2002gl014870, 2003.
- 1021 Hut, G.: Stable Isotope Reference Samples for Geochemical and Hydrological Investigations.  
 1022 Consultant Group Meeting IAEA, Vienna 16–18 September 1985, Report to the Director  
 1023 General, International Atomic Energy Agency, Vienna, 1987.
- 1024 IAEA: Global Network of Isotopes in Rivers, available from: [http://www-](http://www-naweb.iaea.org/napc/ih/IHS_resources_gnir.html)  
 1025 [naweb.iaea.org/napc/ih/IHS\\_resources\\_gnir.html](http://www-naweb.iaea.org/napc/ih/IHS_resources_gnir.html), 2012.
- 1026 IAEA/WMO: Global Network of Isotopes in Precipitation: The GNIP Database, available  
 1027 from: <http://www.iaea.org/water>, 2010.
- 1028 Johnsen, S. J., Dansgaard, W., Clausen, H. B. and Langway, C. C.: Oxygen isotope profiles  
 1029 through the Antarctic and Greenland ice sheets, *Nature*, 235(5339), 429–434, 1972.
- 1030 Johnsen, S. J., Dahl-Jensen, D., Gundestrup, N., Steffensen, J. P., Clausen, H. B., Miller, H.,  
 1031 Masson-Delmotte, V., Sveinbjornsdottir, A. E. and White, J.: Oxygen isotope and  
 1032 palaeotemperature records from six Greenland ice-core stations: Camp Century, Dye-3,  
 1033 GRIP, GISP2, Renland and NorthGRIP, *J. Quat. Sci.*, 16(4), 299–307, 2001.
- 1034 Joussaume, S., Sadourny, R. and Jouzel, J.: A general circulation model of water isotope  
 1035 cycles in the atmosphere, *Nature*, 311(5981), 24–29, 1984.
- 1036 Jouzel, J.: Calibrating the isotopic paleothermometer, *Science*, 286(5441), 910–911, 1999.
- 1037 Jouzel, J.: A brief history of ice core science over the last 50 yr, *CP*, 9(6), 2525–2547, doi:  
 1038 10.5194/cp-9-2525-2013, 2013.
- 1039 Jouzel, J. and Merlivat, L.: Deuterium and oxygen 18 in precipitation: modeling of the  
 1040 isotopic effects during snow formation, *J. Geophys. Res.*, 89(D7), 11749–11575, 1984.
- 1041 Jouzel, J., Russell, G. L., Suozzo, R. J., Koster, R. D., White, J. W. C. and Broecker, W. S.:  
 1042 Simulations of the HDO and H<sub>2</sub><sup>18</sup>O atmospheric cycles using the NASA GISS general  
 1043 circulation model: the seasonal cycle for present-day conditions, *J. Geophys. Res.*,  
 1044 92(D12), 14739–14760, 1987.
- 1045 Jouzel, J., Hoffmann, G., Koster, R. D. and Masson, V.: Water isotopes in precipitation:  
 1046 data/model comparison for present-day and past climates, *Quaternary Sci Rev*, 19(1-5),  
 1047 363–379, 2000.
- 1048 Jouzel, J., Masson-Delmotte, V., Cattani, O., Dreyfus, G., Falourd, S., Hoffmann, G., Minster,  
 1049 B., Nouet, J., Barnola, J. M., Chappellaz, J., Fischer, H., Gallet, J. C., Johnsen, S.,  
 1050 Leuenberger, M., Loulergue, L., Luethi, D., Oerter, H., Parrenin, F., Raisbeck, G.,  
 1051 Raynaud, D., Schilt, A., Schwander, J., Selmo, E., Souchez, R., Spahni, R., Stauffer, B.,

- 1052 Steffensen, J. P., Stenni, B., Stocker, T. F., Tison, J. L., Werner, M. and Wolff, E. W.:  
 1053 Orbital and millennial Antarctic climate variability over the past 800,000 years, *Science*,  
 1054 317(5839), 793–796, doi: 10.1126/science.1141038, 2007.
- 1055 Jungclauss, J. H., Keenlyside, N., Botzet, M., Haak, H., Luo, J. J., Latif, M., Marotzke, J.,  
 1056 Mikolajewicz, U. and Roeckner, E.: Ocean circulation and tropical variability in the  
 1057 coupled model ECHAM5/MPI-OM, *J. Climate*, 19(16), 3952–3972, 2006.
- 1058 Kim, S. T. and O'Neil, J. R.: Equilibrium and nonequilibrium oxygen isotope effects in  
 1059 synthetic carbonates, *Geochim. Cosmochim. Acta*, 61(16), 3461–3475, 1997.
- 1060 Knorr, G., Butzin, M., Micochels, A. and Lohmann, G.: A warm Miocene climate at low  
 1061 atmospheric CO<sub>2</sub> levels, *Geophys. Res. Lett.*, 38(20), doi: 10.1029/2011GL048873, 2011.
- 1062 Kucera, M., Rosell-Mele, A., Schneider, R., Waelbroeck, C. and Weinelt, M.: Multiproxy  
 1063 approach for the reconstruction of the glacial ocean surface (MARGO), *Quaternary Sci*  
 1064 *Rev*, 24(7-9), 813–819, doi: 10.1016/j.quascirev.2004.07.017, 2005.
- 1065 Kurita, N., Noone, D., Risi, C., Schmidt, G. A., Yamada, H. and Yoneyama, K.: Intraseasonal  
 1066 isotopic variation associated with the Madden-Julian Oscillation, *J. Geophys. Res. Atmos.*,  
 1067 116, doi: 10.1029/2010JD015209, 2011.
- 1068 [Lainé, A., Nakamura, H., Nishii, K. and Miyasaka, T.: A diagnostic study of future](#)  
 1069 [evaporation changes projected in CMIP5 climate models, \*Clim. Dyn.\*, 42\(9-10\), 2745–](#)  
 1070 [2761, doi:10.1007/s00382-014-2087-7, 2014.](#)
- 1071 Lee, J.-E., Fung, I., DePaolo, D. J. and Henning, C. C.: Analysis of the global distribution of  
 1072 water isotopes using the NCAR atmospheric general circulation model, *J. Geophys. Res.*  
 1073 *Atmos.*, 112(D16), doi: 10.1029/2006JD007657, 2007.
- 1074 Lee, J.-E., Fung, I., DePaolo, D. J. and Otto-Bliesner, B.: Water isotopes during the Last  
 1075 Glacial Maximum: New general circulation model calculations, *J. Geophys. Res.*,  
 1076 113(D19), D19109, doi: 10.1029/2008JD009859, 2008.
- 1077 Lee, J. E., Pierrehumbert, R., Swann, A. and Lintner, B. R.: Sensitivity of stable water  
 1078 isotopic values to convective parameterization schemes, *Geophys. Res. Lett.*, 36, doi:  
 1079 10.1029/2009gl040880, 2009.
- 1080 LeGrande, A. N. and Schmidt, G. A.: Sources of Holocene variability of oxygen isotopes in  
 1081 paleoclimate archives, *Clim Past*, 5(3), 441–455, 2009.
- 1082 Lehmann, M. and Siegenthaler, U.: Equilibrium oxygen- and hydrogen-isotope fractionation  
 1083 between ice and water, *J. Glaciol.*, 37(125), 23–26, 1991.
- 1084 Lewis, S. C., LeGrande, A. N., Kelley, M. and Schmidt, G. A.: Water vapour source impacts  
 1085 on oxygen isotope variability in tropical precipitation during Heinrich events, *Clim Past*,  
 1086 6(3), 325–343, doi: 10.5194/Cp-6-325-2010, 2010.
- 1087 Lewis, S. C., LeGrande, A. N., Kelley, M. and Schmidt, G. A.: Modeling insights into  
 1088 deuterium excess as an indicator of water vapor source conditions, *J. Geophys. Res.*  
 1089 *Atmos.*, 118(2), 243–262, doi: 10.1029/2012JD017804, 2013.
- 1090 Lohmann, G.: Atmospheric and oceanic freshwater transport during weak Atlantic  
 1091 overturning circulation, *Tellus Series a-Dynamic Meteorology and Oceanography*, 55(5),  
 1092 438–449, 2003.
- 1093 Lorius, C., Merlivat, L., Jouzel, J. and Pourchet, M.: 30,000-Year isotope climatic record  
 1094 from Antarctic ice, *Nature*, 280(5724), 644–648, 1979.
- 1095 Macdonald, R. W., Paton, D. W., Carmack, E. C. and Omstedt, A.: The fresh-water budget  
 1096 and under-ice spreading of Mackenzie River water in the Canadian Beaufort Sea based on  
 1097 salinity and O-18/O-16 measurements in water and ice, *J. Geophys. Res.*, 100(C1), 895–

- 1098 919, doi: 10.1029/94JC02700, 1995.
- 1099 [Maher, B. A. and Thompson, R.: Oxygen isotopes from Chinese caves: records not of](#)  
 1100 [monsoon rainfall but of circulation regime, \*J. Quat. Sci.\*, 27\(6\), 615–624,](#)  
 1101 [doi:10.1002/jqs.2553, 2012.](#)
- 1102 Majoube, M.: Fractionnement en oxygène 18 et en deutérium entre l'eau et sa vapeur, *Journal*  
 1103 *de Chimie et Physique*, 68, 1423–1436, 1971.
- 1104 MARGO Project Members: Constraints on the magnitude and patterns of ocean cooling at the  
 1105 Last Glacial Maximum, *Nature Geoscience*, 2(2), 127–132, doi: 10.1038/Ngeo411, 2009.
- 1106 Marsland, S. J., Haak, H., Jungclaus, J. H., Latif, M. and Roske, F.: The Max-Planck-Institute  
 1107 global ocean/sea ice model with orthogonal curvilinear coordinates, *Ocean Modelling*,  
 1108 5(2), 91–127, 2003.
- 1109 Masson-Delmotte, V., Jouzel, J., Landais, A., Stiévenard, M., Johnsen, S. J., White, J. W. C.,  
 1110 Werner, M., Sveinbjornsdottir, A. and Fuhrer, K.: GRIP deuterium excess reveals rapid  
 1111 and orbital-scale changes in Greenland moisture origin, *Science*, 309(5731), 118–121,  
 1112 2005.
- 1113 Masson-Delmotte, V., Kageyama, M., Braconnot, P., Charbit, S., Krinner, G., Ritz, C.,  
 1114 Guilyardi, E., Jouzel, J., Abe-Ouchi, A., Crucifix, M., Gladstone, R. M., Hewitt, C. D.,  
 1115 Kitoh, A., LeGrande, A. N., Marti, O., Merkel, U., Motoi, T., Ohgaito, R., Otto-Bliesner,  
 1116 B., Peltier, W. R., Ross, I., Valdes, P. J., Vettoretti, G., Weber, S. L., Wolk, F. and Yu, Y.:  
 1117 Past and future polar amplification of climate change: climate model intercomparisons and  
 1118 ice-core constraints, *Clim. Dyn.*, 26(5), 513–529, doi: 10.1007/S00382-005-0081-9, 2006.
- 1119 Merlivat, L. and Jouzel, J.: Global climatic interpretation of the deuterium-oxygen 18  
 1120 relationship for precipitation, *J. Geophys. Res.*, 84(C8), 5029–5033, 1979.
- 1121 Meyer, H., Opel, T., Laepple, T., Dereviagin, A. Y., Hoffmann, K. and Werner, M.: Long-  
 1122 term winter warming trend in the Siberian Arctic during the mid- to late Holocene, *Nature*  
 1123 *Geoscience*, 8(2), 122–125, doi: 10.1038/ngeo2349, 2015.
- 1124 NEEM community members: Eemian interglacial reconstructed from a Greenland folded ice  
 1125 core, *Nature*, 493(7433), 489–494, doi: 10.1038/nature11789, 2013.
- 1126 North Greenland Ice Core Project members: High-resolution record of Northern Hemisphere  
 1127 climate extending into the last interglacial period, *Nature*, 431(7005), 147–151, doi:  
 1128 10.1038/Nature02805, 2004.
- 1129 Paul, A., Mulitza, S. and Pätzold, J.: Simulation of oxygen isotopes in a global ocean model,  
 1130 in: *Use of proxies in paleoceanography: examples from the South Atlantic*, edited by G.  
 1131 Fisher and G. Wefer, pp. 655–686, Springer, Berlin, Heidelberg. 1999.
- 1132 Pfahl, S. and Sodemann, H.: What controls deuterium excess in global precipitation? *Clim*  
 1133 *Past*, 10(2), 771–781, doi: 10.5194/cp-10-771-2014, 2014.
- 1134 Raddatz, T. J., Reick, C. H., Knorr, W., Kattge, J., Roeckner, E., Schnur, R., Schnitzler, K.  
 1135 G., Wetzell, P. and Jungclaus, J.: Will the tropical land biosphere dominate the climate-  
 1136 carbon cycle feedback during the twenty-first century? *Clim. Dyn.*, 29(6), 565–574, doi:  
 1137 10.1007/S00382-007-0247-8, 2007.
- 1138 Risi, C., Bony, S., Vimeux, F. and Jouzel, J.: Water-stable isotopes in the LMDZ4 general  
 1139 circulation model: Model evaluation for present-day and past climates and applications to  
 1140 climatic interpretations of tropical isotopic records, *J. Geophys. Res. Atmos.*, 115(D12),  
 1141 doi: 10.1029/2009JD013255, 2010a.
- 1142 Risi, C., Bony, S., Vimeux, F., Frankenberg, C., Noone, D. and Worden, J.: Understanding  
 1143 the Sahelian water budget through the isotopic composition of water vapor and

- 1144 precipitation, *J. Geophys. Res.*, 115(D24), doi: 10.1029/2010JD014690, 2010b.
- 1145 [Risi, C., Landais, A., Winkler, R. and Vimeux, F.: Can we determine what controls the spatio-](#)  
 1146 [temporal distribution of d-excess and O-17-excess in precipitation using the LMDZ](#)  
 1147 [general circulation model? \*Clim Past\*, 9\(5\), 2173–2193, doi:10.5194/cp-9-2173-2013,](#)  
 1148 [2013.](#)
- 1149 Roche, D. M. and Caley, T.: delta O-18 water isotope in the iLOVECLIM model (version 1.0)  
 1150 - Part 2: Evaluation of model results against observed delta O-18 in water samples, *Geosci.*  
 1151 *Model Dev.*, 6(5), 1493–1504, doi: 10.5194/gmd-6-1493-2013, 2013.
- 1152 Roche, D., Paillard, D., Ganopolski, A. and Hoffmann, G.: Oceanic oxygen-18 at the present  
 1153 day and LGM: equilibrium simulations with a coupled climate model of intermediate  
 1154 complexity, *Earth Planet. Sci. Lett.*, 218(3-4), 317–330, doi: 10.1016/S0012-  
 1155 821x(03)00700-3, 2004.
- 1156 Roche, D. M., Paillard, D., Caley, T. and Waelbroeck, C.: LGM hosing approach to Heinrich  
 1157 Event 1: results and perspectives from data–model integration using water isotopes,  
 1158 *Quaternary Sci Rev*, 106, 247–261, doi: 10.1016/j.quascirev.2014.07.020, 2014.
- 1159 Roeckner, E., Bauml, G., Bonaventura, L., Brokopf, R., Esch, M., Giorgetta, M., Hagemann,  
 1160 S., Kirchner, I., Kornblueh, L., Manzini, E., Rhodin, A., Schlese, U., Schulzweida, U. and  
 1161 Tompkins, A.: The general circulation model ECHAM5. Part I: Model description, Max  
 1162 Planck Institute for Meteorology, Hamburg. 2003.
- 1163 Roeckner, E., Brokopf, R., Esch, M., Giorgetta, M., Hagemann, S., Kornblueh, L., Manzini,  
 1164 E., Schlese, U. and Schulzweida, U.: Sensitivity of simulated climate to horizontal and  
 1165 vertical resolution in the ECHAM5 atmosphere model, *J. Climate*, 19(16), 3771–3791,  
 1166 2006.
- 1167 Rozanski, K., Araguasaraguas, L. and Gonfiantini, R.: Relation between long-term trends of  
 1168 O-18 isotope composition of precipitation and climate, *Science*, 258(5084), 981–985,  
 1169 1992.
- 1170 Schäfer-Neth, C. and Paul, A.: Gridded global LGM SST and salinity reconstruction, doi:  
 1171 10.1029/2006GL029067/full, 2003a.
- 1172 Schäfer-Neth, C. and Paul, A.: The Atlantic Ocean at the Last Glacial Maximum: 1. Objective  
 1173 mapping of the GLAMAP sea-surface conditions, in: *The South Atlantic in the late*  
 1174 *Quaternary - material budget and current systems*, edited by G. Wefer, S. Mulitza, and V.  
 1175 Ratmeyer, pp. 531–548, Springer, Berlin, Heidelberg. 2003b.
- 1176 Schmidt, G. A.: Oxygen-18 variations in a global ocean model, *Geophys. Res. Lett.*, 25(8),  
 1177 1201–1204, 1998.
- 1178 Schmidt, G. A.: Forward modeling of carbonate proxy data from planktonic foraminifera  
 1179 using oxygen isotope tracers in a global ocean model, *Paleoceanography*, 14(4), 482–497,  
 1180 1999.
- 1181 Schmidt, G. A., Bigg, G. R. and Rohling, E. J.: Global seawater oxygen-18 database,  
 1182 available from: <http://www.giss.nasa.gov/data/o18data>, 1999.
- 1183 Schmidt, G. A., LeGrande, A. N. and Hoffmann, G.: Water isotope expressions of intrinsic  
 1184 and forced variability in a coupled ocean-atmosphere model, *J. Geophys. Res.*, 112(D10),  
 1185 doi: 10.1029/2006jd007781, 2007.
- 1186 [Schrag, D. P., Adkins, J. F., McIntyre, K., Alexander, J. L., Hodell, D. A., Charles, C. D. and](#)  
 1187 [McManus, J. F.: The oxygen isotopic composition of seawater during the Last Glacial](#)  
 1188 [Maximum, \*Quaternary Sci Rev\*, 21\(1-3\), 331–342, doi:10.1016/S0277-3791\(01\)00110-X,](#)  
 1189 [2002.](#)

- 1190 Shackleton, N. J.: Attainment of isotopic equilibrium between ocean water and the benthonic  
1191 foraminifera genus *Uvigerina*: isotopic changes in the ocean during the last glacial, Vol.  
1192 219. 1974.
- 1193 Shah, A. M., Morrill, C., Gille, E. P., Gross, W. S., Anderson, D. M., Bauer, B. A., Buckner,  
1194 R. and Hartman, M.: Global speleothem oxygen isotope measurements since the Last  
1195 Glacial Maximum, Dataset Papers in Science, 2013, doi: 10.7167/2013/548048, 2013.
- 1196 [Sharp, Z.: Principles of Stable Isotope Geochemistry, Pearson Prentice Hall, Upper Saddle](#)  
1197 [River, New Jersey, 2007.](#)
- 1198 Steen-Larsen, H. C., Johnsen, S. J., Masson-Delmotte, V., Stenni, B., Risi, C., Sodemann, H.,  
1199 Balslev-Clausen, D., Blunier, T., Dahl-Jensen, D., Ellehøj, M. D., Falourd, S., Grindsted,  
1200 A., Gkinis, V., Jouzel, J., Popp, T., Sheldon, S., Simonsen, S. B., Sjolte, J., Steffensen, J.  
1201 P., Sperlich, P., Sveinbjornsdottir, A. E., Vinther, B. M. and White, J. W. C.: Continuous  
1202 monitoring of summer surface water vapor isotopic composition above the Greenland ice  
1203 sheet, *Atmos. Chem. Phys.*, 13(9), 4815–4828, doi: 10.5194/acp-13-4815-2013, 2013.
- 1204 Steen-Larsen, H. C., Masson-Delmotte, V., Hirabayashi, M., Winkler, R., Satow, K., Prié, F.,  
1205 Bayou, N., Brun, E., Cuffey, K. M., Dahl-Jensen, D., Dumont, M., Guillevic, M.,  
1206 Kipfstuhl, S., Landais, A., Popp, T., Risi, C., Steffen, K., Stenni, B. and Sveinbjornsdottir,  
1207 A. E.: What controls the isotopic composition of Greenland surface snow? *Clim Past*,  
1208 10(1), 377–392, doi: 10.5194/cp-10-377-2014, 2014a.
- 1209 Steen-Larsen, H. C., Sveinbjornsdottir, A. E., Peters, A. J., Masson-Delmotte, V., Guishard,  
1210 M. P., Hsiao, G., Jouzel, J., Noone, D., Warren, J. K. and White, J. W. C.: Climatic  
1211 controls on water vapor deuterium excess in the marine boundary layer of the North  
1212 Atlantic based on 500 days of in situ, continuous measurements, *Atmos. Chem. Phys.*,  
1213 14(15), 7741–7756, doi: 10.5194/acp-14-7741-2014, 2014b.
- 1214 Steen-Larsen, H. C., Sveinbjornsdottir, A. E., Jonsson, T., Ritter, F., Bonne, J. L., Masson-  
1215 Delmotte, V., Sodemann, H., Blunier, T., Dahl-Jensen, D. and Vinther, B. M.: Moisture  
1216 sources and synoptic to seasonal variability of North Atlantic water vapor isotopic  
1217 composition, *J. Geophys. Res. Atmos.*, doi: 10.1002/2015JD023234, 2015.
- 1218 Stenni, B., Masson-Delmotte, V., Johnsen, S., Jouzel, J., Longinelli, A., Monnin, E.,  
1219 Rothlisberger, R. and Selmo, E.: An oceanic cold reversal during the last deglaciation,  
1220 *Science*, 293(5537), 2074–2077, 2001.
- 1221 Stenni, B., Masson-Delmotte, V., Selmo, E., Oerter, H., Meyer, H., Roethlisberger, R., Jouzel,  
1222 J., Cattani, O., Falourd, S., Fischer, H., Hoffmann, G., Iacumin, P., Johnsen, S. J., Minster,  
1223 B. and Udisti, R.: The deuterium excess records of EPICA Dome C and Dronning Maud  
1224 Land ice cores (East Antarctica), *Quaternary Sci Rev*, 29(1-2), 146–159, doi:  
1225 10.1016/J.Quascirev.2009.10.009, 2010.
- 1226 Stepanek, C. and Lohmann, G.: Modelling mid-Pliocene climate with COSMOS, *Geosci.*  
1227 *Model Dev.*, 5(5), 1221–1243, doi: 10.5194/gmd-5-1221-2012, 2012.
- 1228 [Tan, M.: Circulation effect: response of precipitation delta O-18 to the ENSO cycle in](#)  
1229 [monsoon regions of China, \*Clim. Dyn.\*, 42\(3-4\), 1067–1077, doi:10.1007/s00382-013-](#)  
1230 [1732-x, 2014.](#)
- 1231 Thompson, L. G., Davis, M. E., Mosley-Thompson, E., Sowers, T. A., Henderson, K. A.,  
1232 Zagorodnov, V. S., Lin, P. N., Mikhailenko, V. N., Campen, R. K., Bolzan, J. F., Cole-Dai,  
1233 J. and Francou, B.: A 25,000-year tropical climate history from Bolivian ice cores,  
1234 *Science*, 282(5395), 1858–1864, 1998.
- 1235 Thompson, L. G., Mosley-Thompson, E., Davis, M. E., Bolzan, J. F., Dai, J., Yao, T.,  
1236 Gundestrup, N. S., Wu, X., Klein, L. and Xie, Z.: Holocene-Late Pleistocene climatic ice



- 1237 core records from Qinghai-Tibetan Plateau, *Science*, 246, 474–477, 1989.
- 1238 Thompson, L. G., Mosley-Thompson, E., Davis, M. E., Lin, P. N., Henderson, K. A., Coledai,  
1239 J., Bolzan, J. F. and Liu, K. B.: Late glacial stage and Holocene tropical ice core records  
1240 From Huascarán, Peru, *Science*, 269(5220), 46–50, 1995.
- 1241 Thompson, L. G., Mosley-Thompson, E., Davis, M. E., Henderson, K. A., Brecher, H. H.,  
1242 Zagorodnov, V. S., Mashiotta, T. A., Lin, P. N., Mikhalenko, V. N., Hardy, D. R. and  
1243 Beer, J.: Kilimanjaro ice core records: Evidence of Holocene climate change in tropical  
1244 Africa, *Science*, 298(5593), 589–593, 2002.
- 1245 Tian, L., Yao, T., Schuster, P. F., White, J. W. C., Ichiyanagi, K., Pendall, E., Pu, J. and Wu,  
1246 Y.: Oxygen-18 concentrations in recent precipitation and ice cores on the Tibetan Plateau,  
1247 *J. Geophys. Res. Atmos.*, 108(D9), 4293, doi: 10.1029/2002JD002173, 2003.
- 1248 Tindall, J. C., Valdes, P. J. and Sime, L. C.: Stable water isotopes in HadCM3: Isotopic  
1249 signature of El Niño Southern Oscillation and the tropical amount effect, *J. Geophys. Res.*,  
1250 114, doi: 10.1029/2008jd010825, 2009.
- 1251 Uemura, R., Masson-Delmotte, V., Jouzel, J., Landais, A., Motoyama, H. and Stenni, B.:  
1252 Ranges of moisture-source temperature estimated from Antarctic ice cores stable isotope  
1253 records over glacial–interglacial cycles, *Clim Past*, 8(3), 1109–1125, doi: 10.5194/cp-8-  
1254 1109-2012, 2012.
- 1255 Valcke, S., Caubel, A., Declat, D. and Terray, L.: OASIS3 Users’s Guide, CERFACS,  
1256 Toulouse, France. 2003.
- 1257 Vimeux, F., Masson, V., Jouzel, J., Stiévenard, M. and Petit, J. R.: Glacial-interglacial  
1258 changes in ocean surface conditions in the southern hemisphere, *Nature*, 398(6726), 410–  
1259 413, 1999.
- 1260 [Vimeux, F., Gallaire, R., Bony, S., Hoffmann, G. and Chiang, J.: What are the climate](#)  
1261 [controls on  \$\delta D\$  in precipitation in the Zongo Valley \(Bolivia\)? Implications for the Illimani](#)  
1262 [ice core interpretation, \*Earth Planet. Sci. Lett.\*, 240\(2\), 205–220,](#)  
1263 [doi:10.1016/j.epsl.2005.09.031, 2005.](#)
- 1264 Wackerbarth, A., Scholz, D., Fohlmeister, J. and Mangini, A.: Modelling the delta O-18 value  
1265 of cave drip water and speleothem calcite, *Earth Planet. Sci. Lett.*, 299, 387–397, doi:  
1266 10.1016/j.epsl.2010.09.019, 2010.
- 1267 WAIS Divide Project Members: Onset of deglacial warming in West Antarctica driven by  
1268 local orbital forcing, *Nature*, doi: 10.1038/nature12376, 2013.
- 1269 Wang, Y. J., Cheng, H., Edwards, R. L., An, Z. S., Wu, J. Y., Shen, C. C. and Dorale, J. A.: A  
1270 High-Resolution Absolute-Dated Late Pleistocene Monsoon Record from Hulu Cave,  
1271 China, *Science*, 294(5550), 2345–2348, doi: 10.1126/science.1064618, 2001.
- 1272 Wang, Y., Cheng, H., Edwards, R. L., Kong, X., Shao, X., Chen, S., Wu, J., Jiang, X., Wang,  
1273 X. and An, Z.: Millennial- and orbital-scale changes in the East Asian monsoon over the  
1274 past 224,000 years, *Nature*, 451(7182), 1090–1093, doi: 10.1038/Nature06692, 2008.
- 1275 Wei, W. and Lohmann, G.: Simulated Atlantic multidecadal oscillation during the Holocene,  
1276 *J. Climate*, 25(20), 6989–7002, doi: 10.1175/JCLI-D-11-00667.1, 2012.
- 1277 Wei, W., Lohmann, G. and Dima, M.: Distinct modes of internal variability in the global  
1278 meridional overturning circulation associated with the Southern Hemisphere westerly  
1279 winds, *J. Phys. Oceanogr.*, 42(5), 785–801, doi: 10.1175/JPO-D-11-038.1, 2012.
- 1280 Werner, M. and Heimann, M.: Modeling interannual variability of water isotopes in  
1281 Greenland and Antarctica, *J. Geophys. Res.*, 107(D1), 4001, doi: 10.1029/2001JD900253,  
1282 2002.

1283 Werner, M., Mikolajewicz, U., Heimann, M. and Hoffmann, G.: Borehole versus isotope  
1284 temperatures on Greenland: Seasonality does matter, *Geophys. Res. Lett.*, 27(5), 723–726,  
1285 2000.

1286 Werner, M., Heimann, M. and Hoffmann, G.: Isotopic composition and origin of polar  
1287 precipitation in present and glacial climate simulations, *Tellus Ser. B-Chem. Phys.*  
1288 *Meteorol.*, 53(1), 53–71, 2001.

1289 Werner, M., Langebroek, P. M. and Carlsen, T.: Stable water isotopes in the ECHAM5  
1290 general circulation model: Toward high-resolution isotope modeling on a global scale, *J.*  
1291 *Geophys. Res. Atmos.*, doi: 10.1029/2011jd015681, 2011.

1292 Xu, X.: Variations of oceanic and foraminiferal oxygen isotopes at the present day and the  
1293 Last Glacial Maximum: Equilibrium simulations with an oceanic general circulation  
1294 model, Universität Bremen, Alfred-Wegener-Institut, available from:  
1295 <http://hdl:10013/epic.40883>, 2012.

1296 Xu, X., Werner, M., Butzin, M. and Lohmann, G.: Water isotope variations in the global  
1297 ocean model MPI-OM, *Geosci. Model Dev.*, 5(3), 809–818, doi: 10.5194/gmd-5-809-  
1298 2012, 2012.

1299 Yao, T., Thompson, L., Yang, W., Yu, W., Gao, Y., Guo, X., Yang, X., Duan, K., Zhao, H.,  
1300 Xu, B., Pu, J., Lu, A., Xiang, Y., Kattel, D. B. and Joswiak, D.: Different glacier status  
1301 with atmospheric circulations in Tibetan Plateau and surroundings, *Nat Clim Change*, 2(9),  
1302 663–667, doi: 10.1038/nclimate1580, 2012.

1303 Zaucker, F. and Broecker, W. S.: The influence of atmospheric moisture transport on the fresh  
1304 water balance of the Atlantic drainage basin: General circulation model simulations and  
1305 observations, *J. Geophys. Res.*, 97(D3), 2765–2773, doi: 10.1029/91JD01699, 1992.

1306 Zhang, X., Lohmann, G., Knorr, G. and Xu, X.: Different ocean states and transient  
1307 characteristics in Last Glacial Maximum simulations and implications for deglaciation,  
1308 *Clim Past*, 9(5), 2319–2333, doi: 10.5194/cp-9-2319-2013, 2013.

1309 Zhang, X., Lohmann, G., Knorr, G. and Purcell, C.: Abrupt glacial climate shifts controlled  
1310 by ice sheet changes, *Nature*, 512(7514), 290–294, doi: 10.1038/nature13592, 2014.

1311 Zhuang, K. and Giardino, J. R.: Ocean cooling pattern at the Last Glacial Maximum,  
1312 *Advances in Meteorology*, 2012, doi: 10.1155/2012/213743, 2012.

1313

1314

1315 **Table 1:** Selected ice core records, reported PI and  $\Delta(\text{LGM-PI})$  values of  $\delta^{18}\text{O}$  and deuterium  
 1316 excess (dex). No correction for glacial  $\delta^{18}\text{O}$  enrichment has been applied to the listed ice core  
 1317 values. All values are given in permill on the SMOW scale.

1318

Site	Lon	Lat	$\delta^{18}\text{O}_{\text{PI}}$	dex <sub>PI</sub>	$\Delta\delta^{18}\text{O}_{\text{LGM-PI}}$	$\Delta\text{dex}_{\text{LGM-PI}}$
Vostok <sup>1,2</sup>	106.87	-78.47	-57	15.5	-4	-3
Dome F <sup>2,3</sup>	39.70	-77.32	-55	14	-4	-2.5
Dome B <sup>1</sup>	94.92	-77.08	-55	13.5	-5	
EDC <sup>1,4</sup>	123.35	-75.10	-50.9	8.9	-5.4	-3.2
EDML <sup>3,4</sup>	0.07	-75.00	-44.9	4.5	-5	-2.9
Taylor Dome <sup>1</sup>	158.72	-77.80	-38.9	4.9	-3	
Talos <sup>3</sup>	159.18	-72.82	-37.5	3.9	-5	
Byrd <sup>1</sup>	-119.52	-80.02	-32.9	4.5	-8	
Siple Dome <sup>3</sup>	-148.82	-81.67	-26.9	2.9	-8	
WDC <sup>3</sup>	-112.14	-79.46	-34		-8	
GRIP <sup>1</sup>	-37.63	72.58	-35	9.5	-7	-3
NGRIP <sup>1,5</sup>	-42.32	75.10	-35.2		-8	
NEEM <sup>6</sup>	-51.06	77.45			-7.5	
Camp Century <sup>1,7</sup>	-61.13	77.17	-28		-12.9	
Dye3 <sup>8</sup>	-43.81	65.18	-30		-5.5	
Renland <sup>1,8</sup>	-25.00	72.00	-26.5		-5	
Huascarán <sup>1</sup>	-77.61	-9.11			-6.3	-4
Sajama <sup>1</sup>	-68.97	-18.10			-5.4	
Illimani <sup>1</sup>	-67.77	-16.62			-6	-4
Guliyá <sup>1</sup>	81.48	35.28			-5.4	
Dunde <sup>1</sup>	96.00	38.00			-2	

1319

1320 References:

1321 <sup>1</sup>reported in Risi et al. (2010), <sup>2</sup>Uemura et al. (2012), <sup>3</sup>WAIS Divide Project Members (2013),  
 1322 <sup>4</sup>Stenni et al. (2010), <sup>5</sup>North Greenland Ice Core Project members (2004), <sup>6</sup>NEEM community  
 1323 members (2013), <sup>7</sup>Johnsen et al. (1972), <sup>8</sup>Johnsen et al. (2001)

1324

1325 **Table 2:** Selected speleothem sites, reported PI and LGM values of  $\delta^{18}\text{O}_c$  in calcite, and the  
 1326 calculated LGM-PI  $\Delta\delta^{18}\text{O}_{c,\text{LGM-PI}}$  change. All values have been taken from a compilation by  
 1327 Shah et al. (2013) and represent 1,000yrs-averaged  $\delta^{18}\text{O}_c$  values for both the LGM (defined  
 1328 here as period 19,000 to 22,000yrs B.P.) and the most recent 1,000yrs B.P (used as an  
 1329 estimate for  $\delta^{18}\text{O}_{c,\text{PI}}$ ). For Botuverá Cave, Gunung Buda National Park, and Sanbao Cave  
 1330 mean values of several reported speleothem records have been calculated. All  $\delta^{18}\text{O}_c$  values  
 1331 refer to the PDB standard.

1332

Cave Name	Lon	Lat	$\delta^{18}\text{O}_{c,\text{PI}}$ [‰]	$\Delta\delta^{18}\text{O}_{c,\text{LGM-PI}}$ [‰]
Botuverá	-49.16	-27.22	-3.2	-0.3
Cold Air	29.11	-24.02	-4.3	1.2
Gunung Buda	114.80	4.03	-9.3	1.7
Jerusalem West	35.15	31.78	-4.9	1.4
NWSI	172.00	-42.00	-3.2	0.3
Sanbao	110.43	31.67	-8.8	0.1
Sofular	31.93	41.42	-8.1	-4.5
Soreq	35.03	31.45	-5.4	2.2

1333

1334

1335 **Figure Captions**

1336 **Fig. 1. (a)** Global distribution of simulated and observed annual mean  $\delta^{18}\text{O}_p$  values in  
1337 precipitation. The background pattern shows the  $\delta^{18}\text{O}_p$  distribution as simulated by the  
1338 ECHAM5/MPI-OM model setup. Data from 70 GNIP stations (see text), from 21 ice core  
1339 records ~~8 speleothem records~~ (Table 1) and 8 speleothem records ~~16 ice core records~~ (Table  
1340 2) are plotted as coloured symbols. **(b)** Modelled versus observed annual mean  $\delta^{18}\text{O}_p$  at the  
1341 different GNIP, speleothem, and ice cores sites. The black line represents the 1:1 line  
1342 indicating a perfect model fit. **(c)** Observed (black crosses) and modelled (filled red circles)  
1343 spatial  $\delta^{18}\text{O}_p$ -T-relationship for annual mean values of T and  $\delta^{18}\text{O}_p$  at 71 sites, where observed  
1344 annual mean temperatures are below +20°C. The black (red) solid line represents a linear fit  
1345 of the observed (modelled) data set.

1346

1347 **Fig. 2. (a)** Global distribution of simulated and observed annual mean  $\delta^{18}\text{O}_{\text{oce}}$  values in ocean  
1348 surface waters (mean over depth interval between surface and 10m). The background pattern  
1349 shows the  $\delta^{18}\text{O}_{\text{oce}}$  distribution as simulated by the ECHAM5/MPI-OM model setup. Data  
1350 entries from the GISS database are plotted as coloured symbols. **(b)** Anomaly plot for the  
1351 difference of the mean modelled versus observational values ( $\Delta\delta^{18}\text{O}_{\text{oce}} = \delta^{18}\text{O}_{\text{oce}} - \delta^{18}\text{O}_{\text{GISS}}$ ) at  
1352 the positions of the GISS data entries. For the calculation of  $\Delta\delta^{18}\text{O}_{\text{oce}}$ , the month of sampling  
1353 has been considered (see text for details).

1354

1355 **Fig. 3.** Scatter plots of observed present-day  $\delta^{18}\text{O}_{\text{oce}}$  values from the GISS database versus  
1356 modelled  $\delta^{18}\text{O}_{\text{oce}}$  values of the PI simulation for following basins: **(a)** Atlantic Ocean, **(b)**  
1357 Pacific Ocean, **(c)** Indian Ocean, **(d)** Arctic Ocean. The black lines represent the 1:1 line  
1358 indicating a perfect model fit.

1359

1360 **Fig. 4. ~~Background pattern:~~** Meridional section of the simulated  $\delta^{18}\text{O}_{\text{oc}}$  values in **(a)** the  
1361 Atlantic (zonal mean over  $60^\circ\text{W}$  to  $0^\circ\text{W}$ ), **(b)** the Pacific (zonal mean over  $150^\circ\text{E}$  to  $110^\circ\text{W}$ ).  
1362 Data entries from the GISS database for the same regions (Atlantic Ocean:  $n = 5811$ , Pacific  
1363 Ocean:  $n = 2985$ ) are plotted as coloured symbols in panel (c) and (d). ~~For improved~~  
1364 ~~readability, only an arbitrary subset of 300 data entries from the complete available GISS data~~  
1365 ~~set (Atlantic Ocean:  $n = 5811$ , Pacific Ocean:  $n = 2985$ ) is shown in each panel.~~

1366

1367 **Fig. 5.** Global distribution of the simulated annual mean  $\delta^{18}\text{O}_\text{R}$  signal in **(a)** large rivers, **(b)**  
1368 surface water runoff from coastal grid points into the oceans, as simulated by the hydrological  
1369 discharge model (HD model) within the ECHAM5/MPI-OM setup.

1370

1371 **Fig. 6.** Global distribution of simulated and observed annual mean deuterium excess (dex)  
1372 values in **(a)** evaporation, **(b)** precipitation, **(d)** ocean surface waters. The background pattern  
1373 shows the dex distribution as simulated by ECHAM5/MPI-OM. In **(b)**, data from 70 GNIP  
1374 stations, and 21 ice cores from Greenland and Antarctica are plotted as coloured symbols. In  
1375 **(d)**, 153 data entries from the GISS database are plotted as coloured symbols. Comparison of  
1376 observed present-day dex values in **(c)** precipitation (red symbols), and **(e)** in ocean surface  
1377 waters (blue symbols) versus the corresponding modelled dex values of the PI simulation. The  
1378 black lines in **(c)** and **(e)** represent the 1:1 line indicating a perfect model fit.

1379

1380 **Fig. 7. (a)** Background pattern: Simulated global pattern of annual mean surface temperature  
1381 ( $T_{2\text{m}}$ ) changes between the LGM and PI climate. Pollen-based reconstructed temperature  
1382 changes by Bartlein et al. (2011) are shown as coloured symbols. **(b)** Comparison of  
1383 reconstructed temperature changes shown in **(a)** versus the simulated LGM-PI cooling at the  
1384 sample locations. The black line represents the 1:1 line indicating a perfect model fit. **(c)**  
1385 Simulated global pattern of annual mean precipitation changes between the LGM and PI  
1386 climate. **(d)** Comparison of reconstructed precipitation changes shown in **(b)** versus the  
1387 simulated LGM-PI change at the sample locations The black line represents the 1:1 line  
1388 indicating a perfect model fit.

1389

1390 **Fig. 8. (a)** Background pattern: Simulated global pattern of annual mean  $\delta^{18}\text{O}_p$  changes in  
1391 precipitation between the LGM and PI climate. Reconstructed  $\delta^{18}\text{O}_p$  in precipitation changes  
1392 of ice cores (Table 1) and  $\delta^{18}\text{O}_c$  in calcite of ice speleothems (Table 2) are shown as coloured  
1393 symbols. **(b)** Comparison of reconstructed  $\delta^{18}\text{O}$  changes shown in (a) versus the simulated  
1394 LGM-PI  $\delta^{18}\text{O}$  changes at the same locations. Reconstructed  $\delta^{18}\text{O}_p$  anomalies stem from the  
1395 following archives: Antarctica (dark blue), Greenland (light blue), and tropical ice cores  
1396 (grey). For speleothems, reconstructed and simulated  $\delta^{18}\text{O}_c$  changes are shown (green). The  
1397 black line represents the 1:1 line indicating a perfect model fit. **(c)** Histogram of calculated  
1398 temporal LGM-PI  $\delta^{18}\text{O}_p$ -T-gradients for all grid cells with (i) an annual mean PI temperature  
1399 below  $+20^\circ\text{C}$ , and (ii) a simulated LGM-PI cooling of at least  $-2^\circ$ . The dashed line indicates  
1400 the modelled PI spatial  $\delta^{18}\text{O}_p$ -T-gradient ( $0.58\text{‰}/^\circ\text{C}$ ).

1401

1402 **Fig. 9.** Comparison of annual mean LGM  $\delta^{18}\text{O}_p$  anomalies measured in ice cores from  
1403 Antarctica and Greenland (blue bars) versus the simulated ECHAM5/MPI-OM LGM-PI  $\delta^{18}\text{O}_p$   
1404 changes (red bars) at the ice core locations.

1405

1406 **Fig. 10. (a)** Simulated global pattern of annual mean  $\delta^{18}\text{O}_{\text{oce}}$  changes in ocean surface waters  
1407 (0-50m depth) between the LGM and PI climate. **(b)** Calculated global pattern of annual mean  
1408  $\delta^{18}\text{O}_c$  changes in calcite in ocean surface waters between the LGM and PI climate. The  $\delta^{18}\text{O}_c$   
1409 values are derived from the simulated  $\delta^{18}\text{O}_{\text{oce}}$  changes shown in a) and the modelled LGM-PI  
1410 ocean temperature changes (see text for details). **(c)** Difference between simulated LGM-PI  
1411  $\delta^{18}\text{O}_c$  changes and LGM-Late Holocene  $\delta^{18}\text{O}_c$  anomalies of a compilation of 114 planktic  
1412 foraminifera data entries compiled by Caley et al. (2014b).

1413

1414 **Fig. 11.** Background pattern: Meridional section of the simulated annual mean LGM-PI  $\delta^{18}\text{O}_c$   
1415 in calcite changes in **(a)** the Atlantic (zonal over  $60^\circ\text{W}$  to  $0^\circ\text{W}$ ), **(b)** the Pacific (zonal mean  
1416 over  $150^\circ\text{E}$  to  $110^\circ\text{W}$ ). Geographically related data entries from a compilation of 115 LGM-  
1417 Late Holocene  $\delta^{18}\text{O}_c$  anomalies of benthic foraminifera data compiled by Caley et al. (2014b)  
1418 are plotted as coloured symbols (Atlantic Ocean:  $n = 29$ ; Pacific Ocean:  $n = 12$ ) in each panel.

1419

1420 **Fig. 12.** Global distribution of simulated annual mean LGM-PI deuterium excess (dex)  
1421 changes in **(a)** continental precipitation, **(b)** water vapour of the lowest atmospheric model  
1422 layer above the ocean surface.

1423

1424 **Fig. 13.** Comparison of annual mean LGM dex anomalies measured in ice cores from  
1425 Antarctica and Greenland (blue bars) versus simulated LGM-PI dex changes (ECHAM5/MPI-  
1426 OM: red bars; ECHAM5-wiso: light grey bars) at the ice core locations

1427

1428 **Fig. 14.** Relation between simulated LGM-PI deuterium excess (dex) changes of Southern  
1429 Hemisphere water vapour of the lowest atmospheric model layer above the ocean surface  
1430 versus simulated LGM-PI changes of **(a)** relative humidity above the Southern Hemisphere  
1431 ocean surface (rh; red symbols); **(b)** Southern Hemisphere sea surface temperatures (SST,  
1432 blue symbols).

1433